

The effect of wall roughness on two-phase flow in a rough-walled Hele-Shaw cell

A. A. Alturki · B. B. Maini · I. D. Gates

Received: 16 March 2013 / Accepted: 4 November 2013 / Published online: 28 November 2013
© The Author(s) 2013. This article is published with open access at Springerlink.com

Abstract Many studies focus on the flow of multiple phases in smooth fractures yet most real fractures are rough thus flow regime maps and results for multiphase flow in smooth fractures are not completely applicable to flow in rough fractures. The effect of wall roughness is difficult to understand in multiphase flow in fractures since it leads to heterogeneities of the fracture aperture and potentially alters the roles of capillary and viscous forces in the flow. Here, the effects of wall roughness, fracture orientation, and fluids flow direction within a fracture, modeled as narrow gap in a Hele-Shaw cell, on co-current flow of oil and water were examined. The results are presented in the form of oil and water relative permeability curves. The results demonstrate that roughness impacts phase distribution, flow regimes, and phase relative permeability (a measure of phase interference); roughness increases oil–water phase interference and hysteresis of the flow resistance when scanning up and down in water saturation. Fractal analysis of images of the phase arrangement in the fracture reveals that the fractal dimension (reflects geometry and complexity), lacunarity (gappiness and complexity), and tortuosity relate the complexity of flow and the change in relative permeability behavior. The experimentally derived relative permeability data were fitted to the saturation exponent model and to an equivalent homogenous single-phase model.

Keywords Fracture · Hele-Shaw · Two-phase flow · Oil–water system · Fractal dimension · Lacunarity · Tortuosity

List of symbols

A	Flow cross-sectional area, m^2
C	Impedance parameter
D_B	2D boxing counting fractal dimension
D_h	Hydraulic diameter of fracture, m
e	Saturation exponent
g	Gravitational acceleration, m/s^2
h	Fracture aperture, m
k	Absolute permeability, m^2
k_r	Relative permeability
L	Length of test section, m
n	Constant
Δp	Pressure gradient, Pa
p	Pressure, Pa
Q	Volumetric flow rate, m^3/s
Re	Reynolds number
S_{or}	Residual oil saturation
S_{wi}	Initial water saturation
S_{wirr}	Irreducible water saturation
V	Volumetric flux, m^3/s
W	Hele-Shaw cell's (fracture) width, m
μ	Dynamic viscosity, Pa s
π	Fracture (pipe) perimeter, m
ψ	Friction factor, Nm
ρ	Density, kg/m^3
λ	Lacunarity
τ	Channel tortuosity
θ	Inclination angle

Subscripts

g	Gas phase
l	Liquid
m	Mixture
o	Oil phase
w	Water phase

A. A. Alturki (✉) · B. B. Maini · I. D. Gates
Chemical and Petroleum Engineering Department, Schulich
School of Engineering, University of Calgary, 2500 University
Drive NW, Calgary, AB T2N1N4, Canada
e-mail: ali.turki.2@aramco.com; ali.alturki@gmail.com

Introduction

One of the most commonly used definitions for a natural fracture within a rock is given by Aguilera (1995) as follows “a discontinuity that results from stresses that exceed the rupture strength of the rock”. In carbonate oil reservoirs, a rock fracture is a planar-shaped void filled with oil, water, gas, and/or rock fines. Those fractures may span from micron-scale microfractures to large-scale faults that span tens to hundreds of meters (Aguilera 1995). Usually, fractures of variable scales co-exist forming networks of fractures that connect and thus have an effective permeability as a network. In oil-bearing fractured rock reservoirs, relative to the rock matrix, fractures are often highly permeable flow pathways that dominate fluid flow within the reservoir and production to the surface (Aguilera 1995; Chen and Horne 2006; Shad et al. 2010). Studies of multiphase flow in fractures are scarce and the majority of studies focus on single- or two-phase flow in a single smooth-walled fracture, in other words, multiphase flow in what is effectively a Hele-Shaw cell (Fourar and Bories 1995; Pan et al. 1996; Shad et al. 2010). However, outcrop studies show that fractures are often rough with variable aperture thus the application of multiphase flow results obtained from smooth-walled model fractures are approximations to flow in real fractures. There are several studies on gas–liquid flow in roughened model fractures; however, there are very few dealing with liquid–liquid flow in such systems. Here, we focus on oil and water flow in a roughened-wall Hele-Shaw cell to examine the effect of roughness on phase distributions, flow regime, and phase interference. Phase interference and other physics like wall roughness and pore structure is represented by phase relative permeability curves and reflects capillary and viscous interactions of the two phases within the fracture. If there is no interference of one phase by the other, then the relative permeability curves of each phase should be straight. The larger the phase interference, the more curved is the

relative permeability curves and the larger is the “residual” immobile phase saturation (fraction of volume of the gap occupied by a phase is referred to as the phase saturation) within the fracture.

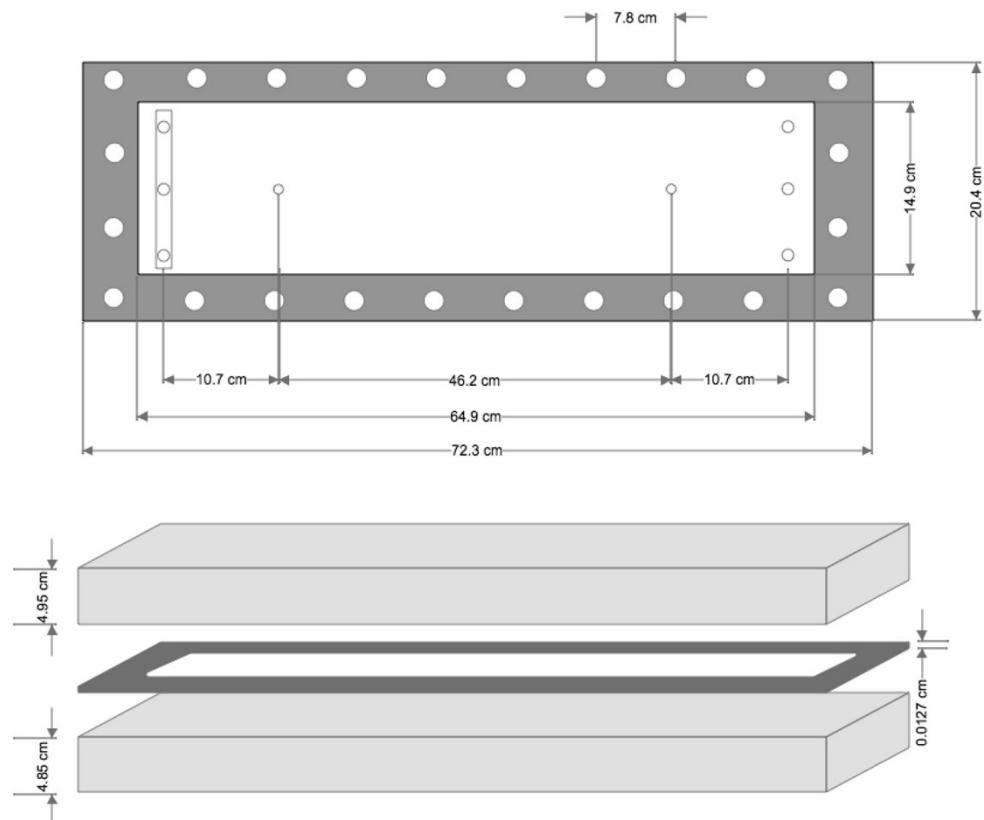
Fourar et al. (1993) conducted air–water flow experiments in three horizontal rough-walled fractures. In one of the models, the two surfaces (plates) were in contact whereas in the other two, the surfaces were separated using a spacer (gasket). The surface roughness was established by applying a 0.3-mm-thick layer of epoxy cement and gluing a layer of 1 mm in diameter glass beads on both glass plates. The water saturation was calculated using the volume balance method. They found that the experimental relative permeability to air and water is not linearly dependent on the saturation. The best data fit to the experimental data was obtained by the homogenous single-phase model (HSPM). The HSPM approximates two-phase flow by a single-phase approximation where the single-phase effective properties are determined from the properties of the two phases. Similar to flow in pipes, a correlation between the friction factor and average Reynolds number was used to predict the pressure drop in each model configuration. Persoff and Pruess (1995) evaluated the flow of gas and water through a natural rough-walled rock fracture and three transparent epoxy resin replica models. Relative permeability measurements indicated phase interference between the two phases. This was counter to the view (which is adapted in some reservoir engineering and numerical simulation applications) that relative permeability of each phase is equal to its saturation, that is, the relative permeability curves are straight with no immobile phase saturations. Diomampo (2001) conducted a study on the relative permeability of nitrogen–water system in a rough-walled fracture. A smooth-walled model was roughened by inserting a wire mesh between glass (top) and aluminum (bottom) plates. Similar to the smooth-walled fracture, each phase traveled through the fracture in a localized continuous flow path, however, the stability of the path heavily depended on the nitrogen–water flow rate ratio. At low gas–water ratios, invading water blocked the gas path, leaving behind discontinuous gas bubbles. In contrast to this, more stable and wide flow paths of gas were formed at high gas–water flow rate ratios. The data fit obtained using the homogeneous single-phase model did not provide a satisfactory representation of nitrogen–water flow in the fracture. However, she observed similar flow structures on both the smooth- and rough-walled fractures, which differ from the flow structures suggested by Fourar and Bories (1995). Chen and Horne (2004), and Chen (2005) found that the flow structures of gas and water flow in rough-walled fracture is more scattered and tortuous compared to the ones observed with the smooth-walled fracture. Also, they observed phase trapping

Table 1 Properties of oil (MARCOL-7) and deionized-degassed dyed water

Property	MARCOL-7 Value	Dyed water Value
Grade	N & N3 NF	NA
Density at 22 °C, kg/m ³	850	998.78
Viscosity at 22 °C, mPa s	21	1.1080
Kinematic viscosity at 40 °C	12.8E–6	1.1094E–6
Reflective Index	1.466	NA
σ_{ow} at 22 °C, mN/m	16	
Surface tension at 22 °C, mN/m	25	
Contact angle of oil–water interface on Plexiglass, °	84	

Table 2 Experimental cases

Case	Gap, cm	Flow direction	Inclination	Number of points at which relative permeability evaluated	Range of flow rate ratios
Model-I					
1	0.0381	Horizontal	Horizontal	83	1:0.1...1:2,750...1:0.1
2	0.0381	Up-dip	90°	83	1:0.1...1:2,750...1:0.1
3	0.0381	Down-dip	90°	83	1:0.1...1:2,750...1:0.1
Model-II					
4	0.125	Horizontal	Horizontal	83	1:0.1...1:2,750...1:0.1
5	0.125	Up-dip	30°	83	1:0.1...1:2,750...1:0.1
6	0.125	Up-dip	60°	83	1:0.1...1:2,750...1:0.1
7	0.125	Up-dip	90°	83	1:0.1...1:2,750...1:0.1
8	0.125	Down-dip	30°	83	1:0.1...1:2,750...1:0.1
9	0.125	Down-dip	60°	83	1:0.1...1:2,750...1:0.1
10	0.125	Down-dip	90°	83	1:0.1...1:2,750...1:0.1
11	0.125	Horizontal	Horizontal	59	1:0.1...1:220...1:0.1
12	0.125	Up-dip	90°	59	1:0.1...1:220...1:0.1
13	0.125	Down-dip	90°	59	1:0.1...1:220...1:0.1

Fig. 1 Rough-walled Hele-Shaw cell dimensions

of gas and water due to fracture aperture variations and to capillary pressure effects. Steam and water flow in smooth-walled fracture demonstrated multiple unstable flow patterns whereas in the nitrogen and water system, each phase tended to form its own flow path with blocking and unblocking by the other phase. Chen and Horne (2006)

defined channel tortuosity to quantify the flow paths created by each phase in rough-walled fractures. They found that the magnitude of the flow channel tortuosity increases when the heterogeneity of the fracture increases. Pan (1999) studied oil–water flow in rough-walled fractures. His apparatus consisted of two plates of roughened

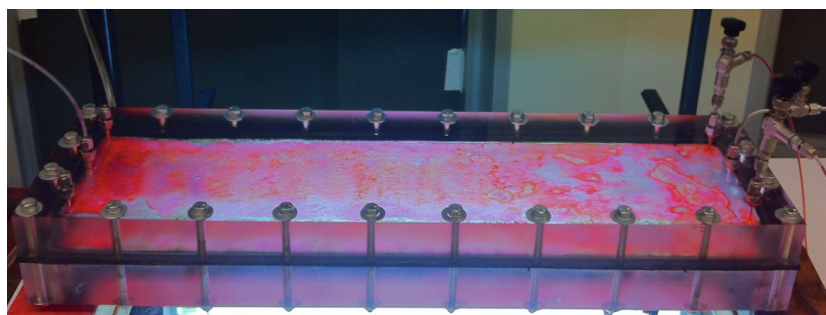
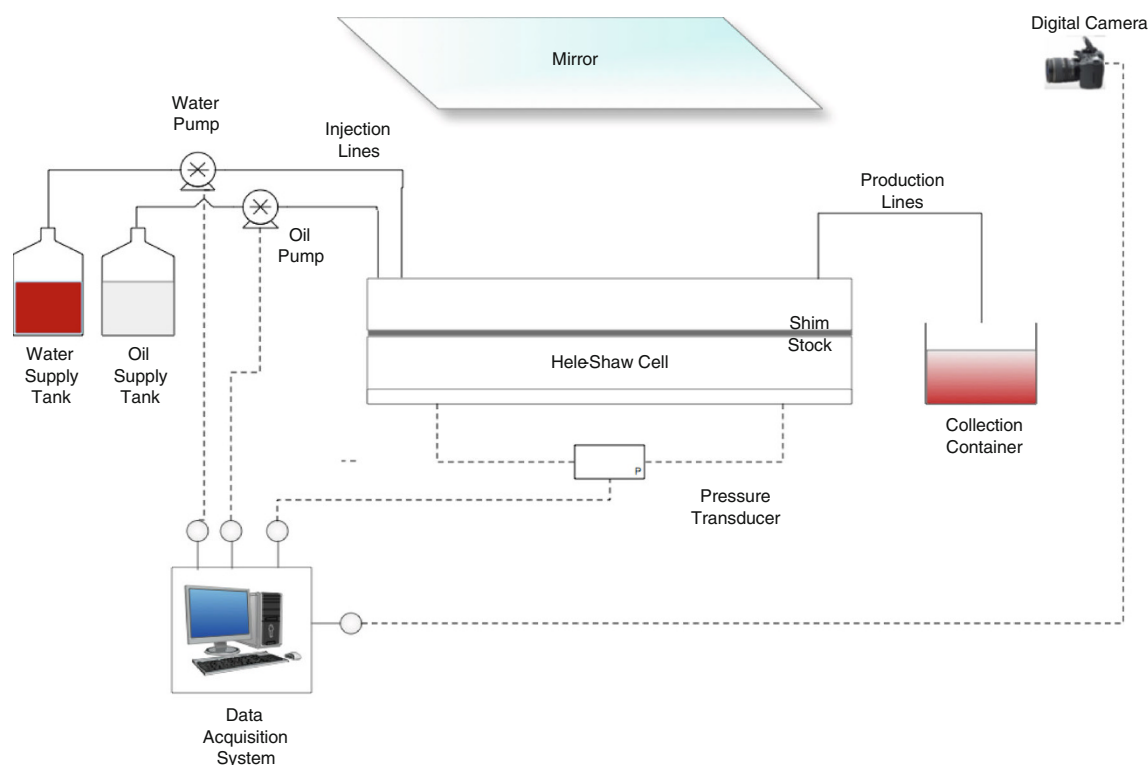


Fig. 2 Schematic of Hele-Shaw experimental apparatus

Plexiglas. The roughness was created by gluing glass beads of known mesh size on both inner faces of the two plates. Shim stock of varying thickness was inserted at the periphery for fracture aperture adjustment. Over all of the conditions of his experimental runs, he observed a dispersed flow regime and found that the relative permeability of oil is a function of oil saturation, viscosity ratio, and flow pattern whereas the relative permeability to water depends mostly on water saturation. The effects of surface roughness on relative permeability to oil and water were more pronounced for smaller fracture aperture and at higher pressure gradient, i.e., the relative permeabilities and flow patterns observed in the rough-walled fracture with larger aperture were similar to the ones observed with the smooth-walled fracture. The results of previous

experimental studies of multiphase flow in roughened model fracture demonstrates that the flow structure is complex and that capillary pressure effects and flow path tortuosity affect phase trapping and, consequently, relative permeability, that is, phase flow interference occurs.

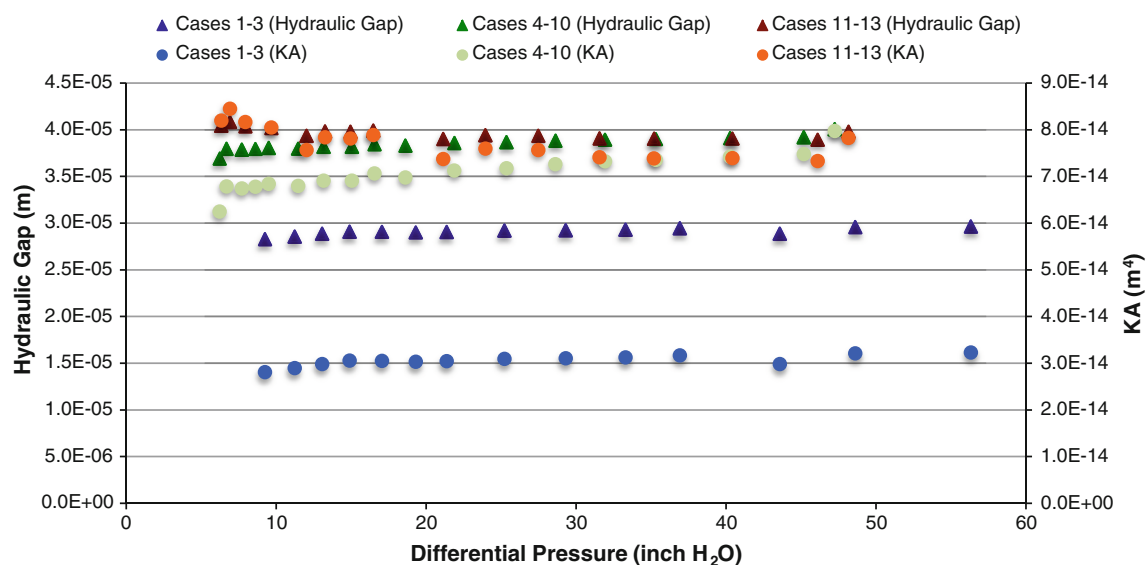
Experimental setup and procedure

Fluid properties

Table 1 lists the properties of the fluids used in the experiments. The wetting phase is a colorless mineral oil (MARCOL-7, Imperial Oil). Degassed-deionized dyed water is used as the non-wetting phase. Water-based super-

Table 3 Homogenous single-phase model (HSPM) and saturation exponent model (SEM) parameters

Case	Inclination, flow direction	HSPM		Saturation exponent model			
		C, Impedance parameter		n_o		n_w	
		IWIR (drainage)	DWIR (imbibition)	IWIR (drainage)	DWIR (imbibition)	IWIR (drainage)	DWIR (imbibition)
Model-I							
1	Horizontal	0.5355	0.6035	2.50	0.50	1.21	1.18
2	90° up-dip	0.6819	0.6832	3.20	0.50	1.20	1.5
3	90° down-dip	0.2414	0.2797	2.50	2.50	1.21	1.19
Model-II							
4	Horizontal	0.4242	0.4682	0.79	0.50	2.61	1.20
5	30° up-dip	0.5756	0.6154	0.50	0.3	3.00	1.50
6	60° up-dip	0.6661	0.6528	0.50	0.30	3.00	0.50
7	90° up-dip	0.5397	0.6291	0.50	0.5	3.00	0.80
8	30° down-dip	0.3652	0.2880	1.50	0.60	3.00	2.15
9	60° down-dip	0.3065	0.2385	2.12	0.56	3.00	7.29
10	90° down-dip	0.2782	0.2240	3.00	0.50	3.00	0.80
11	Horizontal	0.4011	0.3799	0.50	0.40	3.57	1.12
12	90° up-dip	0.4978	0.2955	0.70	0.25	7.36	0.50
13	90° down-dip	0.2733	0.2609	0.29	0.40	2.60	1.40

**Fig. 3** Hydraulic fracture aperture (m) and KA (m⁴) measurements with differential pressure (inches H₂O)

red food coloring (Chefmaster Airbrush Color, Super Red) is used to dye the water to make it more opaque to better visualize and analyze the images.

Physical model apparatus

The plates of the Hele-Shaw cells were constructed from Plexiglas. The inner faces of the plates were machined, cleaned, and then roughened by applying an adhesive on both inner faces of the two plates onto which glass beads

(US standard sieve #80; sieve opening 0.177 mm) were randomly sprayed. Variable thickness Teflon shims are used as spacers to set the nominal gap between the two plates. Two gaps were examined: in Model-I, the nominal gap was set equal to 0.0381 cm whereas in Model-II, it was set to 0.125 cm (Table 2). A torque of 40.6 Nm (30 ft.lb) is applied on bolts to put the plates together and seal the Teflon shim-stock gasket.

Three injection and three production ports were drilled on the sides of the upper plate. The oil (wetting phase) is

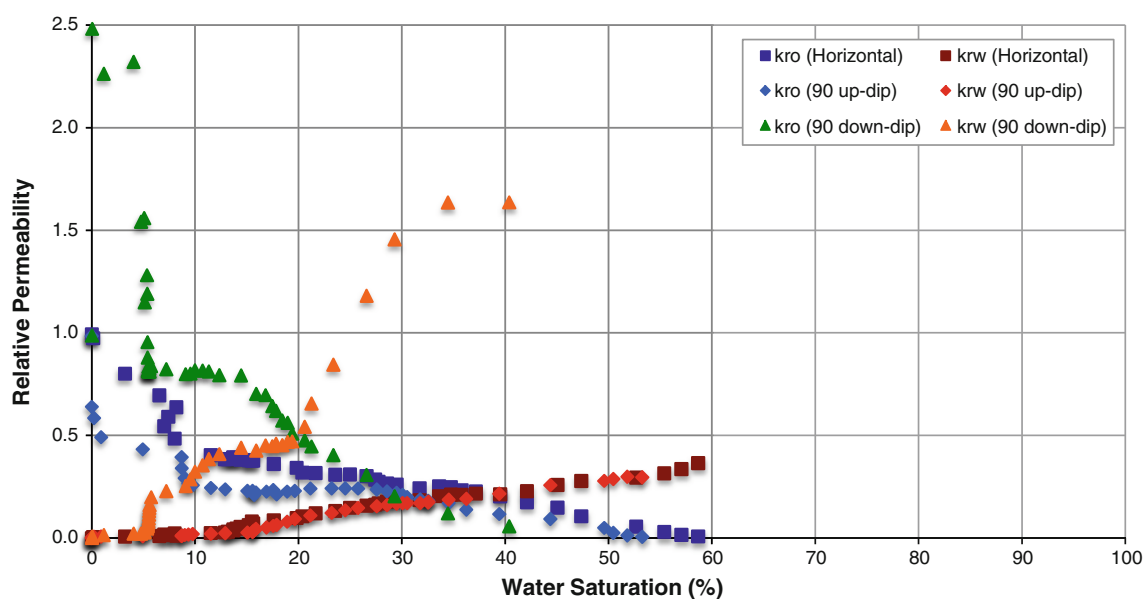


Fig. 4 IWIR process relative permeability curves with respect to oil and water for Cases 1–3

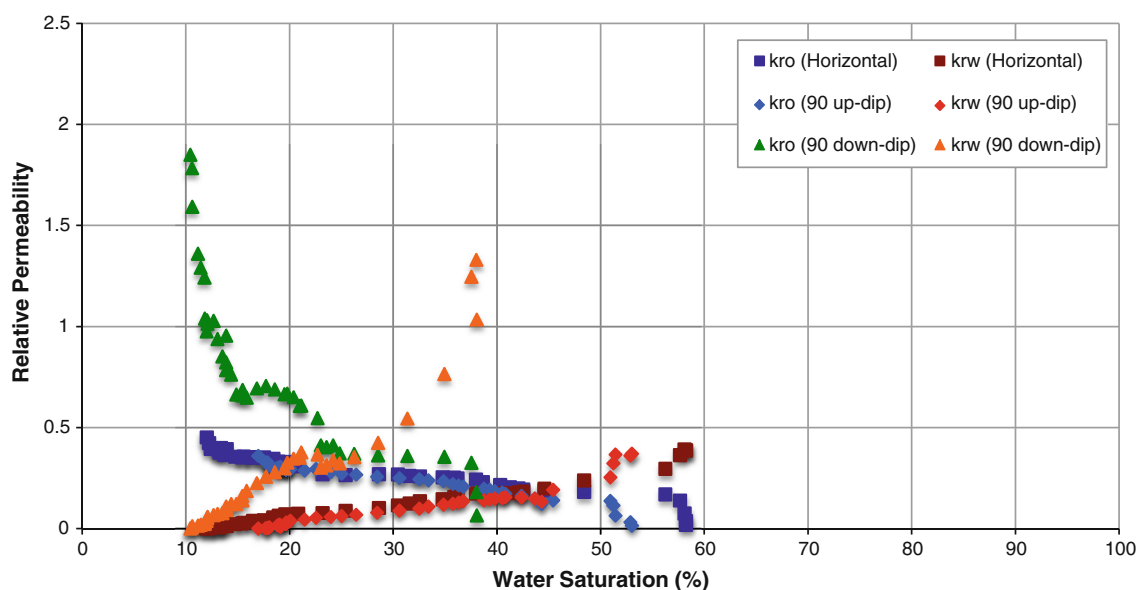


Fig. 5 DWIR process relative permeability curves with respect to oil and water for Cases 1–3

injected through the side injection ports whereas water (non-wetting phase) is injected through the middle port. To measure the pressure drop across the model, two pressure taps were drilled at the bottom plate connected to the pressure transducer. Figure 1 shows the relative locations of the injection/production ports and the two pressure taps. Figure 2, also, shows a simplified schematic of the experiment setup and a photograph of the Hele-Shaw cell. A height adjustment lever and stand were used to place the Hele-Shaw cell and the light source in the desired inclination.

The data acquisition system (LabView 2009, National Instruments) was used to record and analyze the data. The pressure transducers and oil and water pumps are connected to the data acquisition system providing the pressure difference across the flow cell, and oil and water flow rates. The oil and water saturations in the gap were calculated from the high-resolution images obtained with a digital camera (Blaster scA1000-30fc, Vision Technology) and acquired by the data acquisition system.

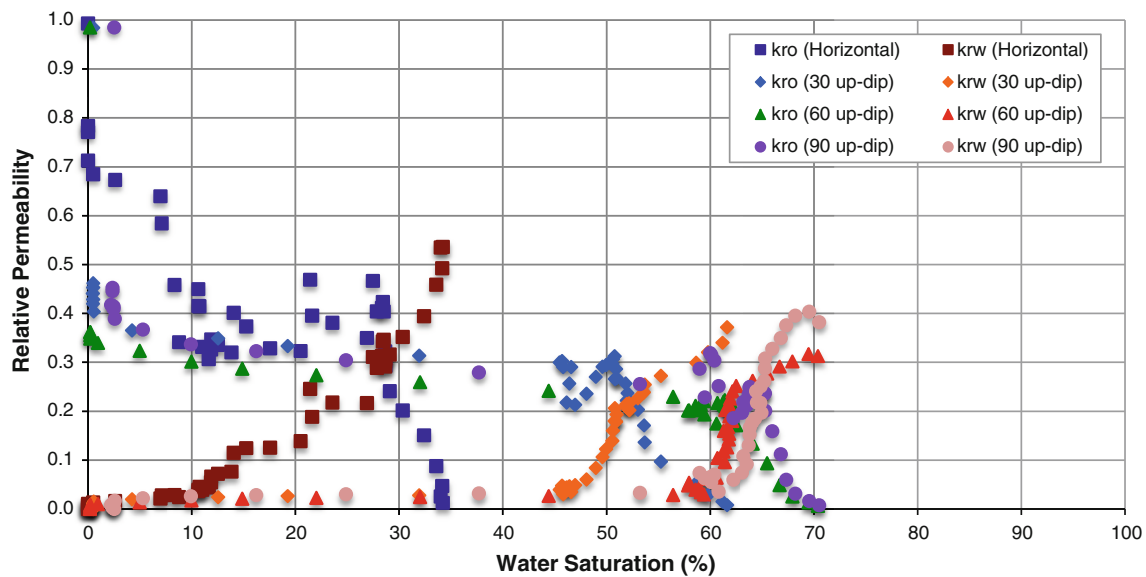


Fig. 6 IWIR process relative permeability curves with respect to oil and water for Cases 4–7—up-dip flow direction

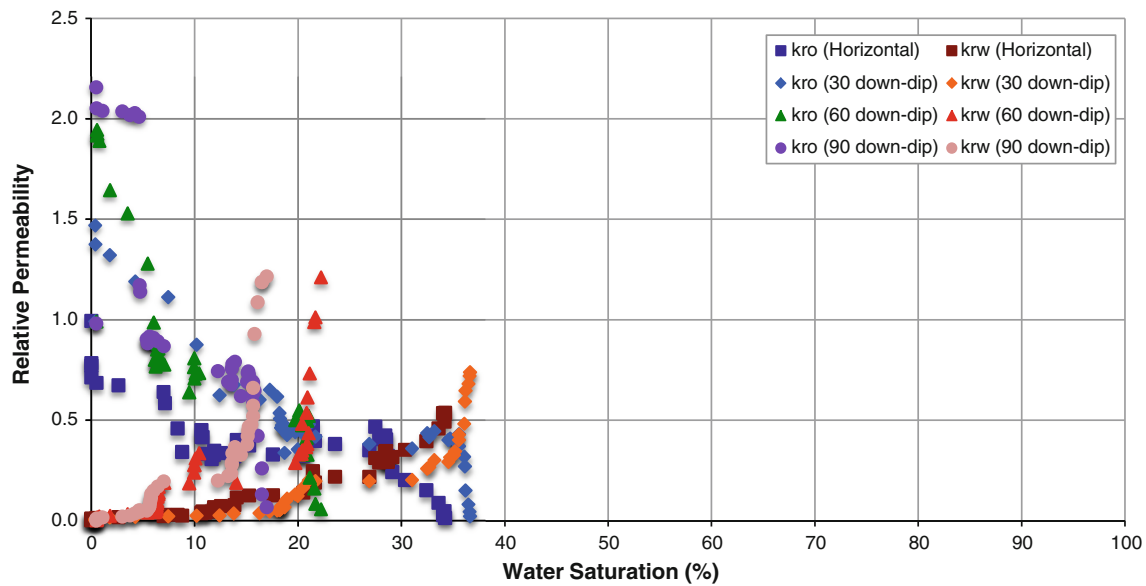


Fig. 7 IWIR process relative permeability curves with respect to oil and water for Cases 4 and 8–10—down-dip flow direction

Experimental procedure

At both gaps, a number of inclination angles were examined: 0° (horizontal), 30°, 60°, and 90° with the flow direction being up-dip in one set of experiments and down-dip for another set. In all experiments, the gap was initially filled with oil (wetting phase). The absolute permeability was determined from single-phase flow experiments. Table 3 lists the total number of experimental cases conducted. In Cases 1–10, initially, water (non-wetting phase) was injected co-currently at 10:1 oil-to-water volumetric flow rate ratio.

As the experiment progressed, the fractional flow of water was increased and after reaching an oil-to-water flow ratio equal to 1:2,750 (the period over which the water rate was raised will be referred to as the Increasing Water Injection Rate, IWIR, period), the operation was reversed and the water flow rate was decreased stepwise back to oil-to-water flow rate ratio equal to 10:1 (the period over which the water rate was reduced will be referred to as the Decreasing Water Injection Rate, DWIR, period). In Cases 11–13, the process is reversed after the oil-to-water flow ratio reached a value equal to 1:220, i.e., traversing back through the oil–water

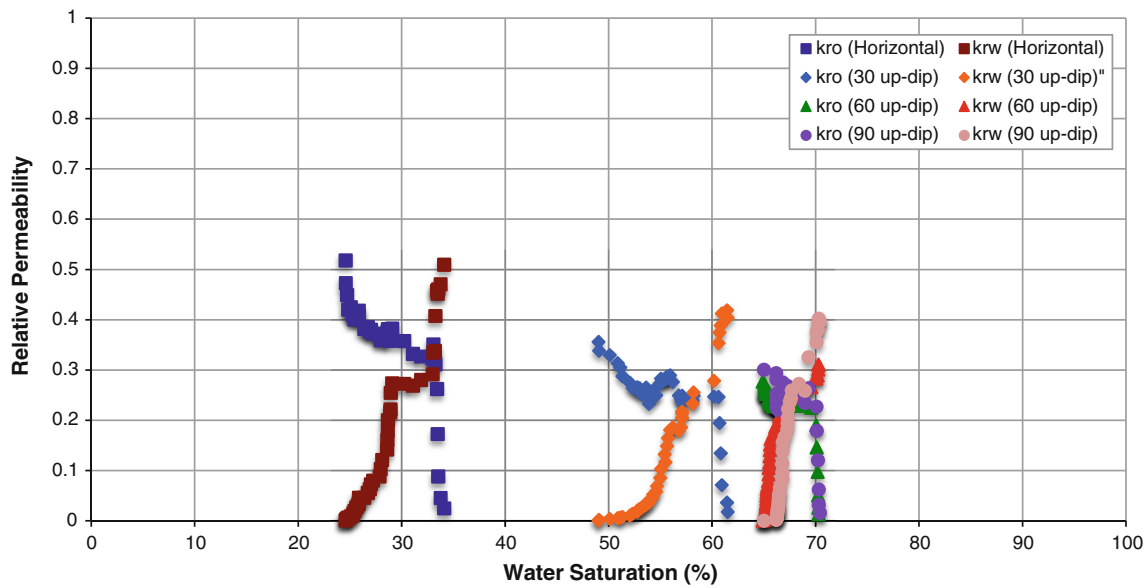


Fig. 8 DWIR process relative permeability curves with respect to oil and water in Cases 4–7—up-dip flow direction

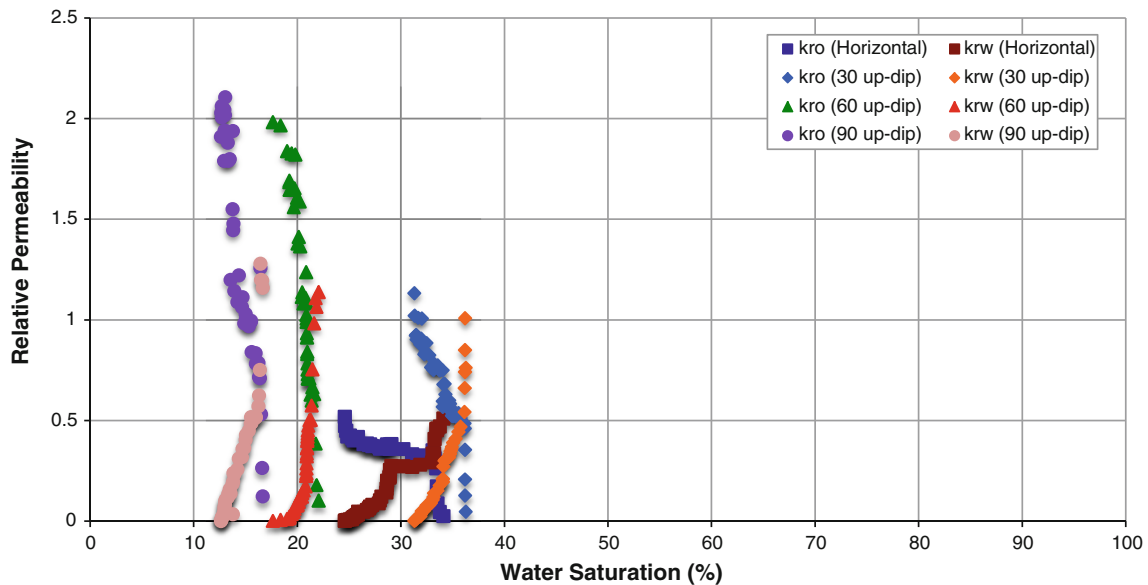


Fig. 9 DWIR process relative permeability curves with respect to oil and water in Cases 4 and 8–10—up-dip flow direction

flow rater ratios in a stepwise fashion. Figures 12 and 13 show a series of images for Case 1 during IWIR and DWIR processes, respectively. The flow was considered to have reached a pseudo-steady state after the pressure difference stabilized for 5 min. Depending on the flow rate, this period took between 5 and 15 min to establish.

Fracture aperture measurements

For perfectly smooth plates, parallel laminar steady flow within the gap under a pressure gradient is given by:

$$\frac{Q}{A} = \frac{h^2}{12\mu} \frac{\Delta p}{L} \quad (1)$$

where Q/A is the volumetric flux (Q is the volumetric flow rate and A is the cross-sectional area open to flow), h is the gap, μ is the fluid viscosity, and dp/L is the pressure gradient in the direction of flow. From an equivalence to Darcy's law, given by:

$$\frac{Q}{A} = \frac{k\Delta p}{\mu L} \quad (2)$$

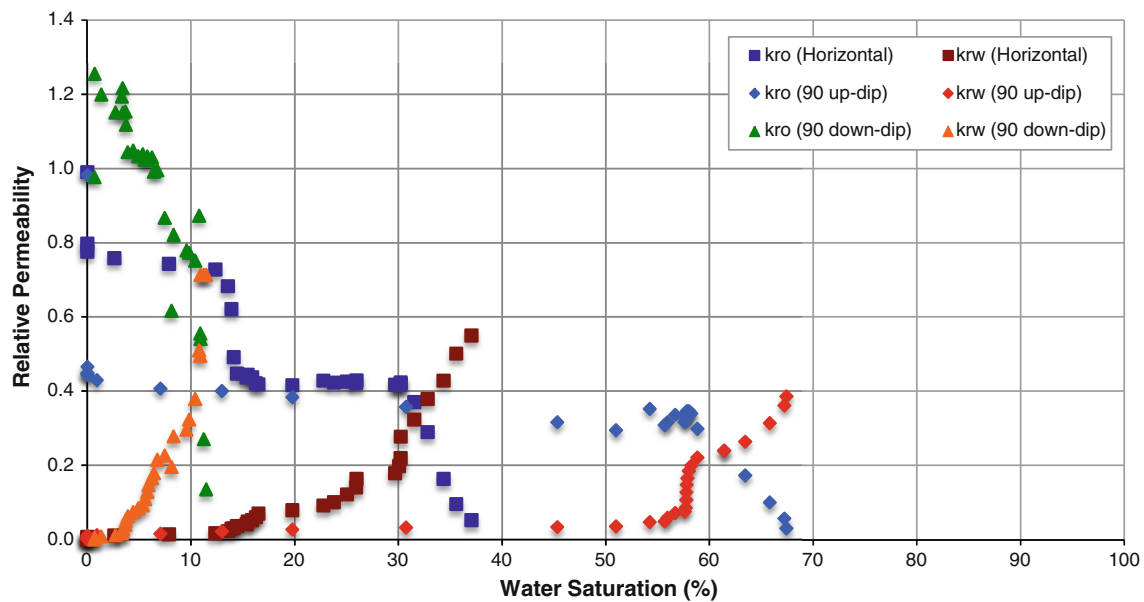


Fig. 10 IWIR process relative permeability curves with respect to oil and water in Cases 11–13

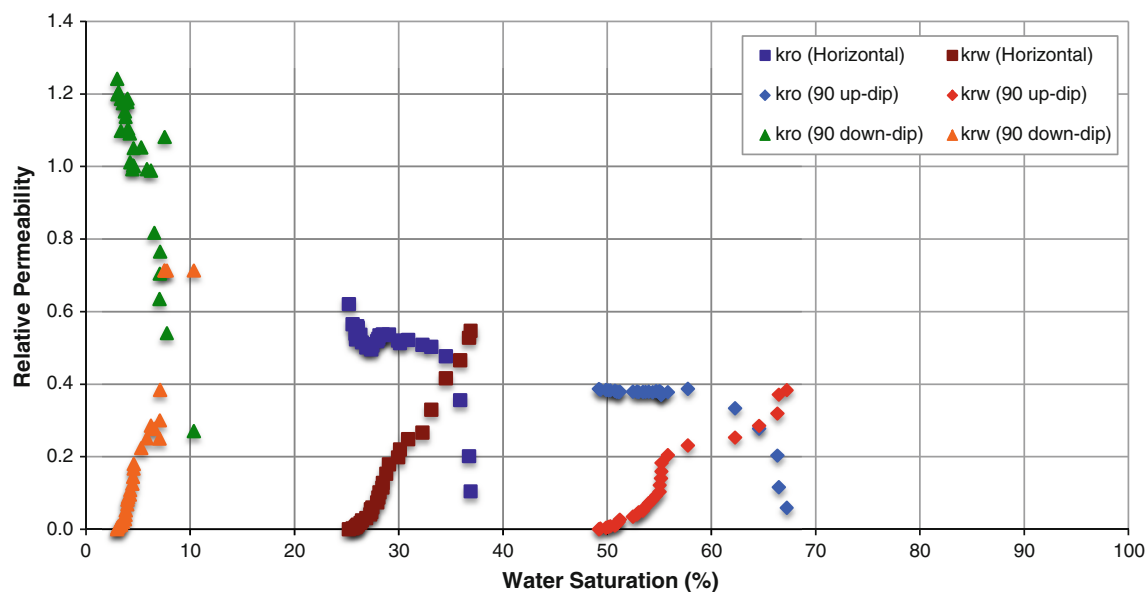


Fig. 11 DWIR process relative permeability curves with respect to oil and water in Cases 11–13

The absolute permeability of the gap, k , is equal to:

$$k = \frac{h^2}{12} \quad (3)$$

Therefore, if $A = hW$, where W is the width of the flow area, the effective gap can be determined by:

$$h = \sqrt[3]{\frac{12Q\mu L}{W\Delta p}} \quad (4)$$

Figure 3 shows measurements of the gap and product of absolute permeability and cross-sectional area open to flow, kA , versus differential pressure (Δp) measured

in inches of water (laminar, single-phase flow). The data shows minimal gap sensitivity to pressure in the fracture.

Results

Relative permeability data

The relative permeability to oil and water is calculated using Darcy's law. The relative permeability with respect to oil is given by:



Fig. 12 Oil (transparent)–water (red) flow structure evolution in Case 1 during the IWIR process (Q_o and Q_w are expressed in ml/min, and S_w is a percentage). Flow direction is from right to left



Fig. 12 continued

$$k_{ro} = \frac{Q_o \mu_o}{A k_{abs} \left(\frac{\Delta p}{L} + \Delta \rho g \sin \theta \right)}$$

(5) where $\Delta \rho$ is the density difference of the wetting and non-wetting phases and g is the acceleration due to gravity. The relative permeability with respect to water is equal to:



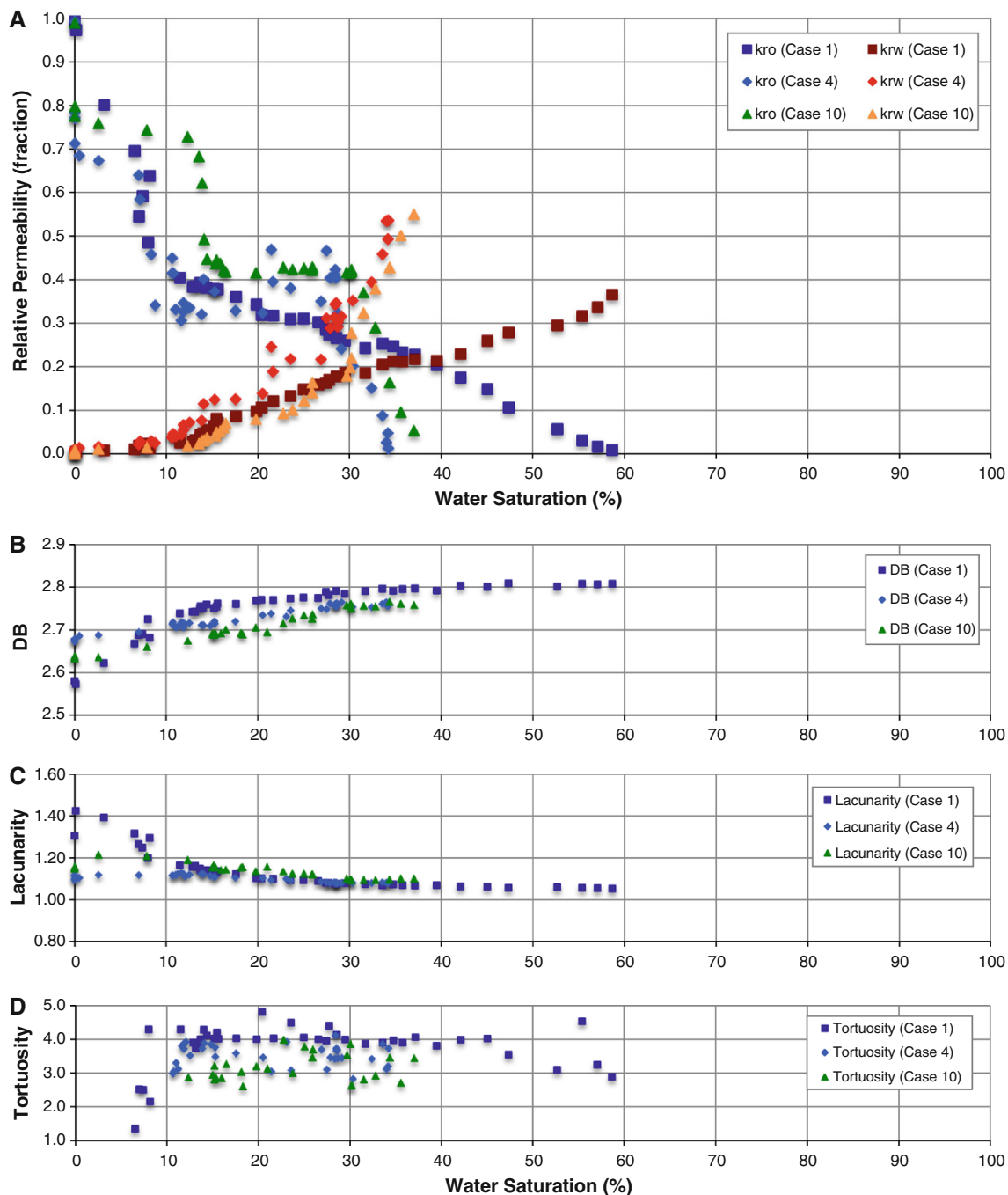
Fig. 13 Oil (transparent)–water (red) flow structure evolution in Case 1 during the DWIR process (Q_o and Q_w are expressed in ml/min, and S_w is a percentage). Flow direction is from *right to left*



Fig. 13 continued

Table 4 Fracture walls' roughness measurements

	Root mean square (Rq) (microinch)	Arithmetic average (Ra) (microinch)	Skewness (Rsk)	Kurtosis (Rku)	Highest peak (Rp)	Lowest valley	Total height
Cases 1–3	205.635	204.004	1.021	1.053	250	13	263.000
Cases 4–10	196.866	192.178	1.058	1.146	254.667	8.687	263.333
Cases 11–13	200.488	196.860	1.044	1.111	254.000	9.333	263.333

**Fig. 14** **a** IWIR process relative permeability curves with respect to oil and water in horizontal rough-walled cases, **b** box counting dimension, D_B , **c** lacunarity, λ , **d** channel tortuosity, τ

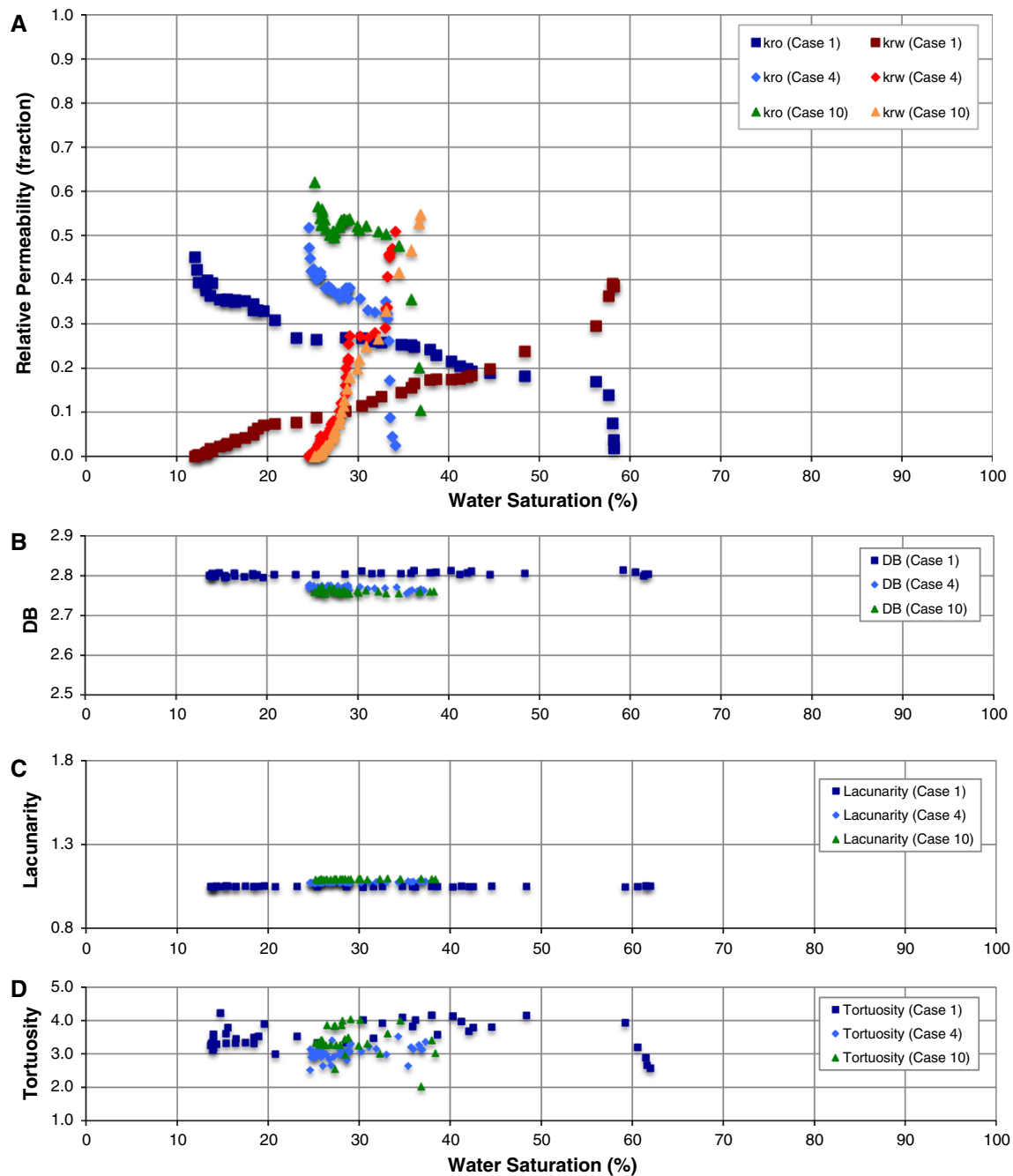


Fig. 15 **a** DWIR process relative permeability curves with respect to oil and water in horizontal rough-walled cases, **b** box counting dimension, D_B , **c** lacunarity, λ , **d** channel tortuosity, τ

$$k_{rw} = \frac{Q_w \mu_w}{A k_{abs} \frac{4p}{L}} \quad (6)$$

In Eq. (6), the gravity term is not added when calculating the relative permeability to water since the tubes connected to the differential pressure transducers are filled with water, and therefore, the hydrostatic head is accounted for in the transducers readings for the water phase. Figures 4 and 5

show, respectively, the relative permeability measurements to oil and water for Cases 1–3 (nominal gap = 0.0381 cm, maximum injected water-to-oil ratio = 1:2,750). The up- and down-dip flow IWIR relative permeabilities of Cases 4–10 (gap = 0.125 cm, maximum injected water-to-oil ratio = 1:2,750) are depicted in Figs. 6 and 7 whereas, the DWIR ones are depicted in Figs. 8 and 9. Finally, Figs. 10 and 11, respectively, depict the IWIR and DWIR data

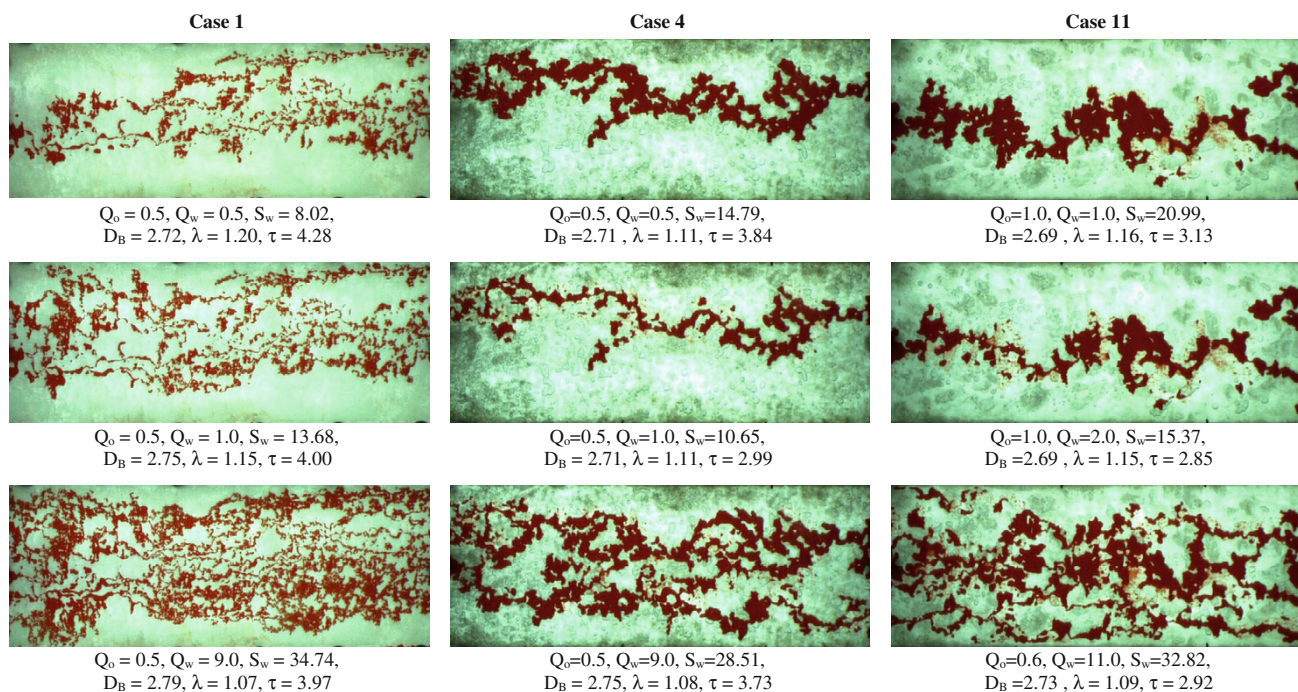


Fig. 16 Two-phase (oil is transparent, water is red) flow distributions in Cases 1, 4, and 11 during IWIR process (Q_o and Q_w are expressed in ml/min, and S_w is a percentage)

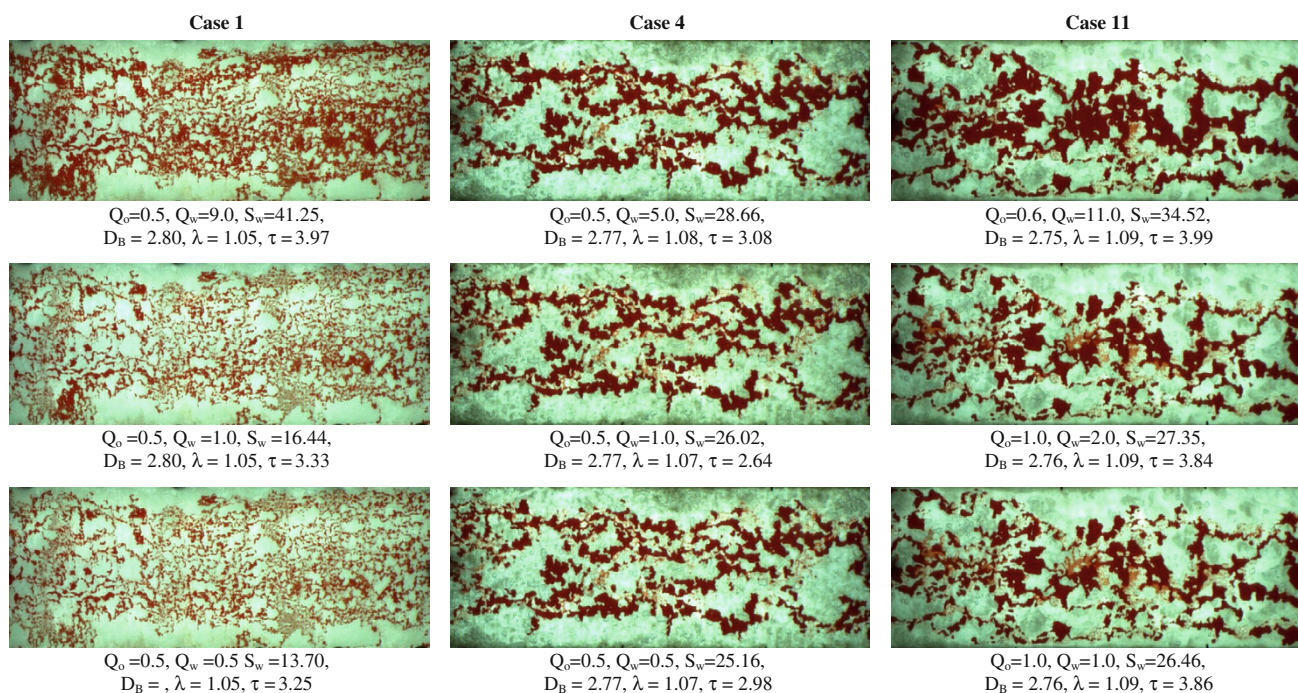


Fig. 17 Two-phase (oil is transparent, water is red) flow distributions in Cases 1, 4, and 11 during DWIR process (Q_o and Q_w are expressed in ml/min, and S_w is a percentage)

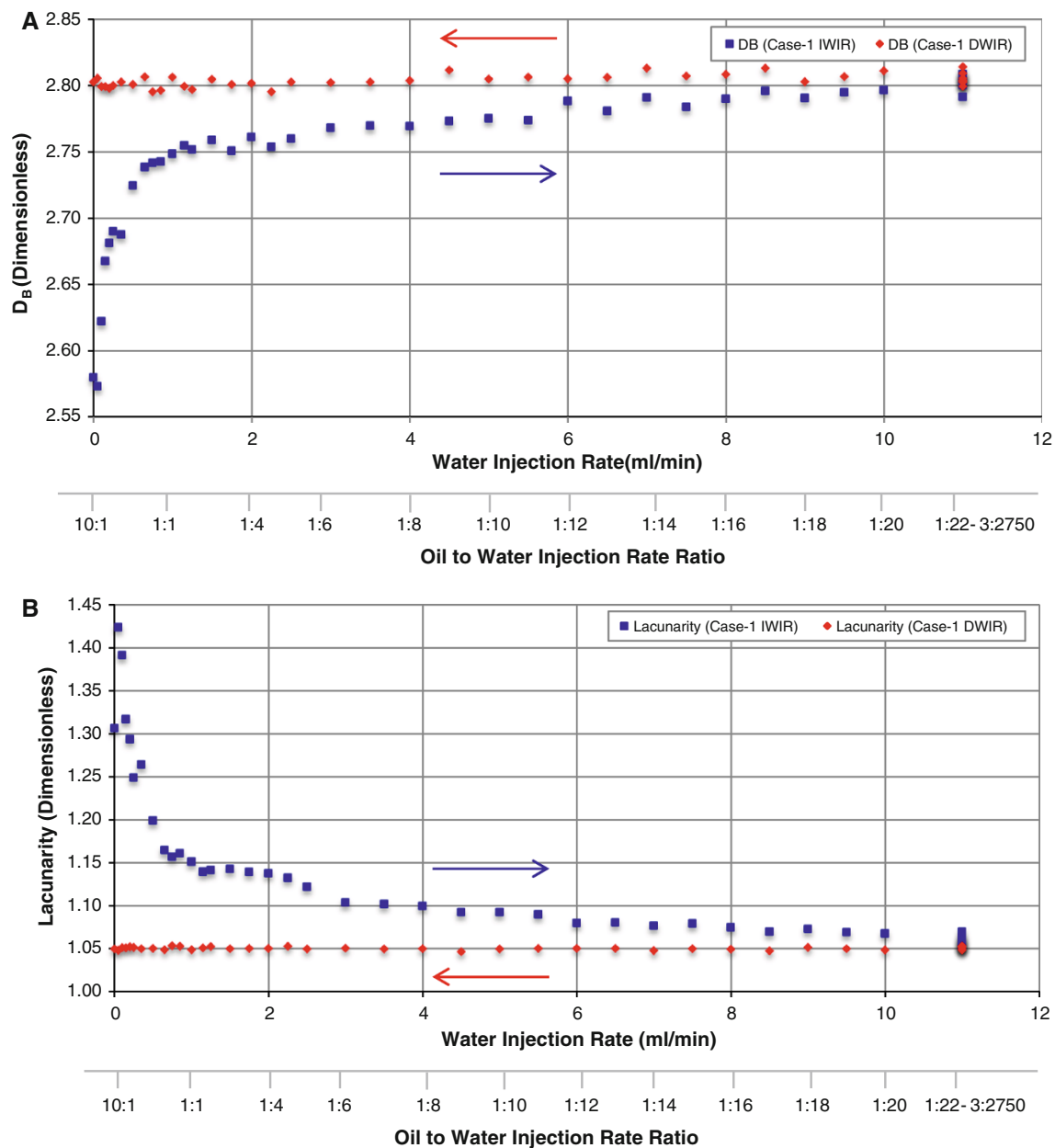


Fig. 18 Multiple flow states and hysteresis in Case 1: **a** fractal dimension, D_B and **b** lacunarity, λ

obtained from Cases 11–13 (gap = 0.125 cm, maximum injected water-to-oil ratio = 1:220).

Flow structure

Unlike the smooth-walled Hele-Shaw cells, only channel flow was observed with the rough-walled gap. Figures 12 and 13 show snapshots of the co-current flows of oil and water during IWIR period and DWIR period processes, respectively, for Case 1 (horizontal orientation). It has been observed that the channels intensity and width varies between the three models due to the different gaps. A closer look at the snapshots taken for Case 1 shows the

formation of water pockets that grow larger with increasing water saturation.

Surface roughness, fractal dimension, lacunarity, and tortuosity

Table 4 lists roughness measurements for the fracture configurations under consideration. The high-resolution images taken throughout the experiments were processed and evaluated for fractal dimension, lacunarity, and channel tortuosity. Fractal dimension (D_B) is a measure of complexity indicating the extent of change in details with change in scale. Sometimes, digital images may result in

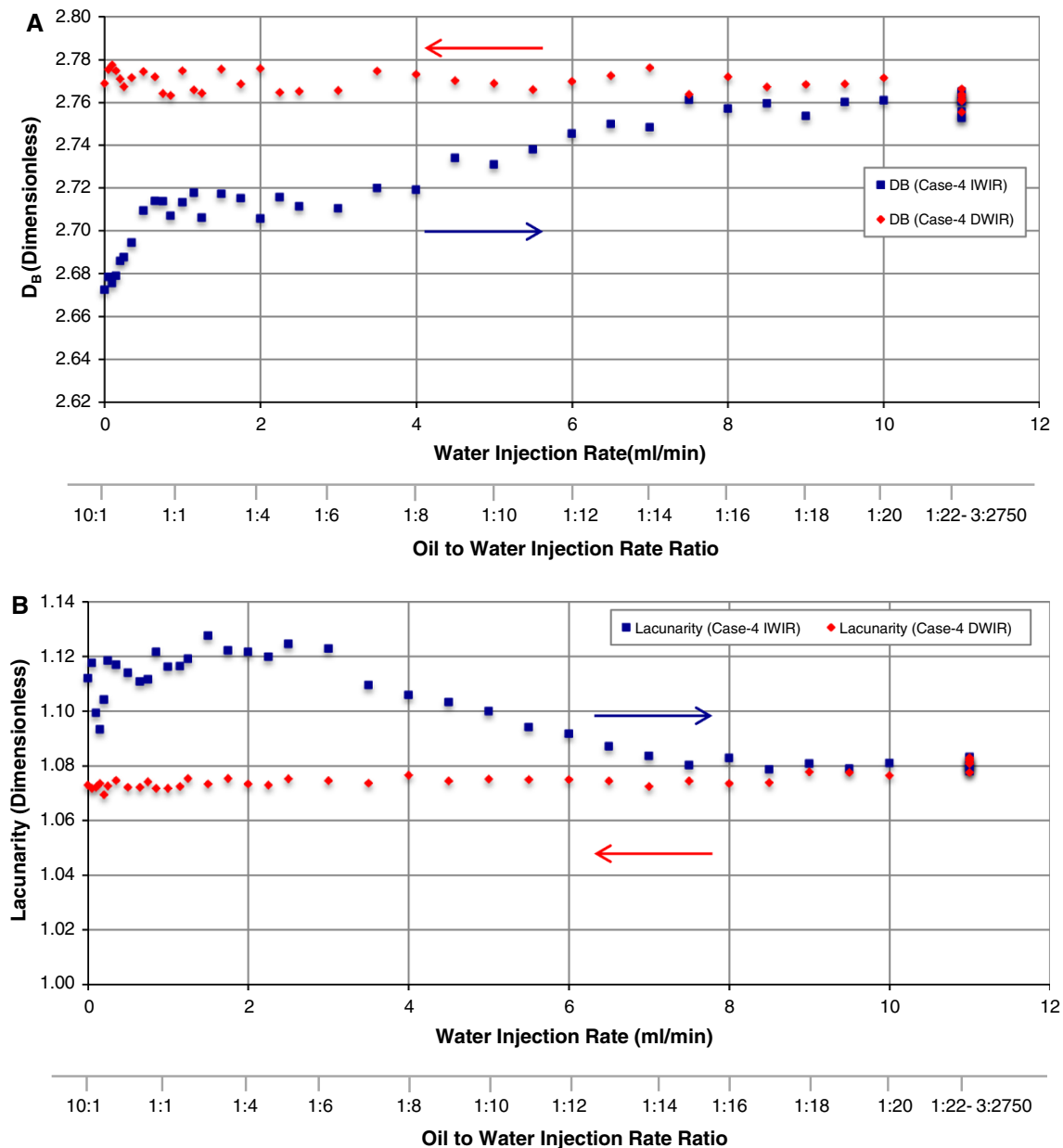


Fig. 19 Multiple flow states and hysteresis in Case 4: **a** fractal dimension, D_B and **b** lacunarity, λ

close or even identical fractal dimensions. Lacunarity (λ) is an additional parameter that is needed to make that distinction. It is a measure of the gappiness, texture, and heterogeneity of the objects in the image. Both D_B and λ reported in this work are based on the box counting method used by the ImageJ image processing software (National Institutes of Health, Bethesda, MD, USA, <http://rsb.info.nih.gov/ij/>) and the “FracLac” plugin. In addition, the “AnalyzeSkeleton” plugin was used to assess the tortuosity of the water channels. The tortuosity is defined by:

$$\tau = \left(\frac{L_e}{L} \right)^2 \quad (7)$$

where, L_e is the channel length and L is length of the test section between the inlet and outlet pressure taps. Figures 14 and 15 show IWIR and DWIR experimental relative permeability for all cases together with fractal dimensions, lacunarity, and water channel tortuosity versus water saturation in the gap.

Figure 14 shows D_B , λ , and τ for Cases 1, 4, and 10 corresponding to each experimental relative permeability point at a given water saturation. The results reveal that D_B enlarged with increasing water saturation and decreasing k_{ro} and increasing k_{rw} values. The lacunarity values imply the increasing complexity of the flow with decreasing

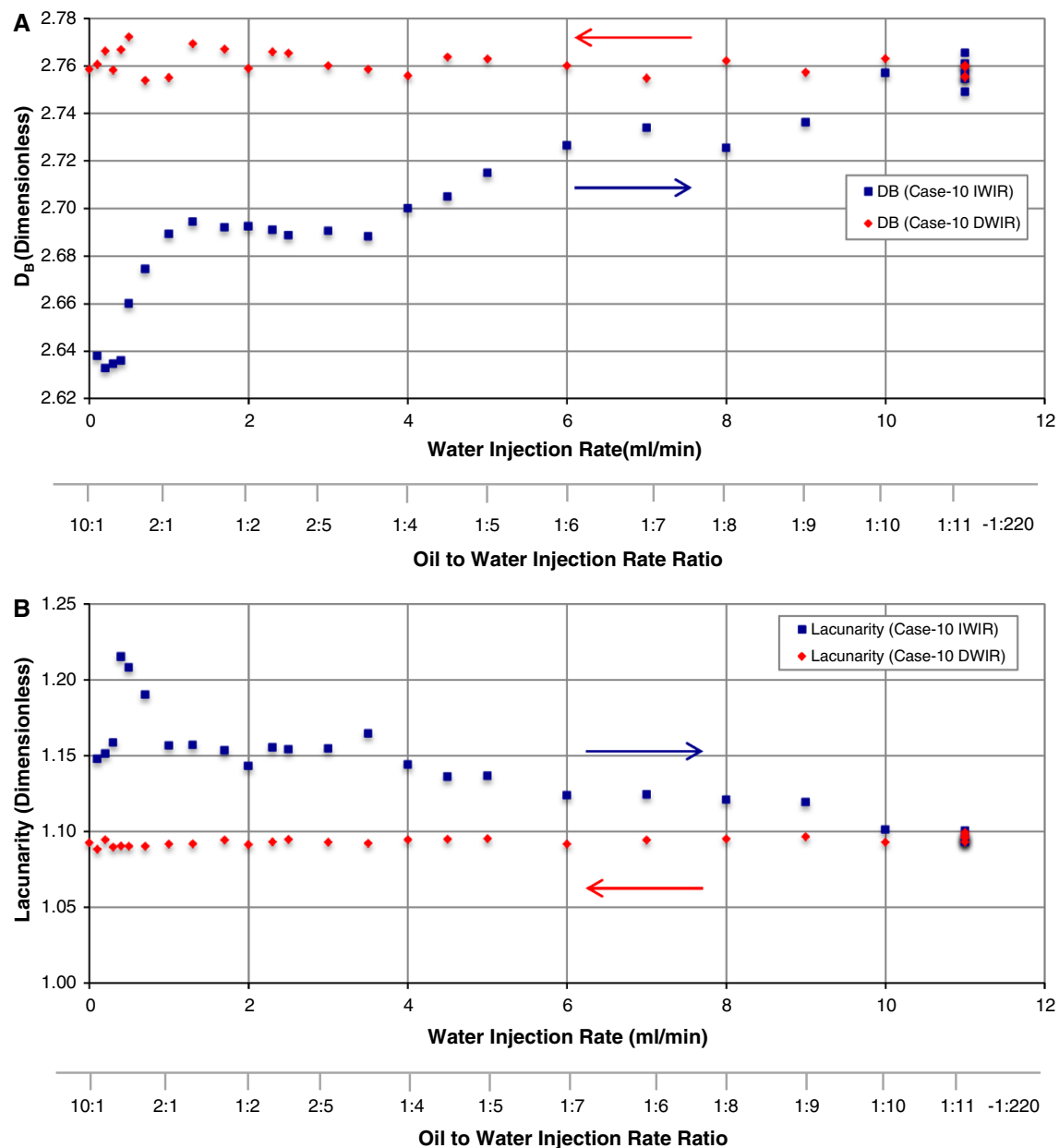


Fig. 20 Multiple flow states and hysteresis in Case 11: **a** fractal dimension, D_B and **b** lacunarity, λ

spatial extent of the oil phase and multi-channeling of water phase. Case 1 shows slightly higher tortuosity values due the smaller fracture aperture and higher surface roughness compared to Cases 4 and 8. Figure 15 shows the irreversible nature of the process with DWIR. Figures 16 and 17 show images of flow in Cases 1, 4, and 10 at the same flow rate ratios during IWIR and DWIR, respectively. Clearly, the dominating flow regime is channel flow; however, each of the cases demonstrates its version of the complexity associated with two-phase flow in a roughened gap. The relative permeability data, and the complex and tortuous flow channels suggest the presence of phase interference and phase trapping as is observed with two-

phase flow in porous media. Figures 18, 19 and 20 show the effect of the hysteresis on the flow. In addition to the clear evidence of hysteresis on relative permeability data, the fractal analysis shows different paths of complexity for IWIR and DWIR periods. At any given oil-to-water flow rate ratio, there are at least two states by which the system can be described.

Data matching with model predictions

The empirical saturation exponent model (SEM) and the homogenous single-phase model (HSPM) were both used

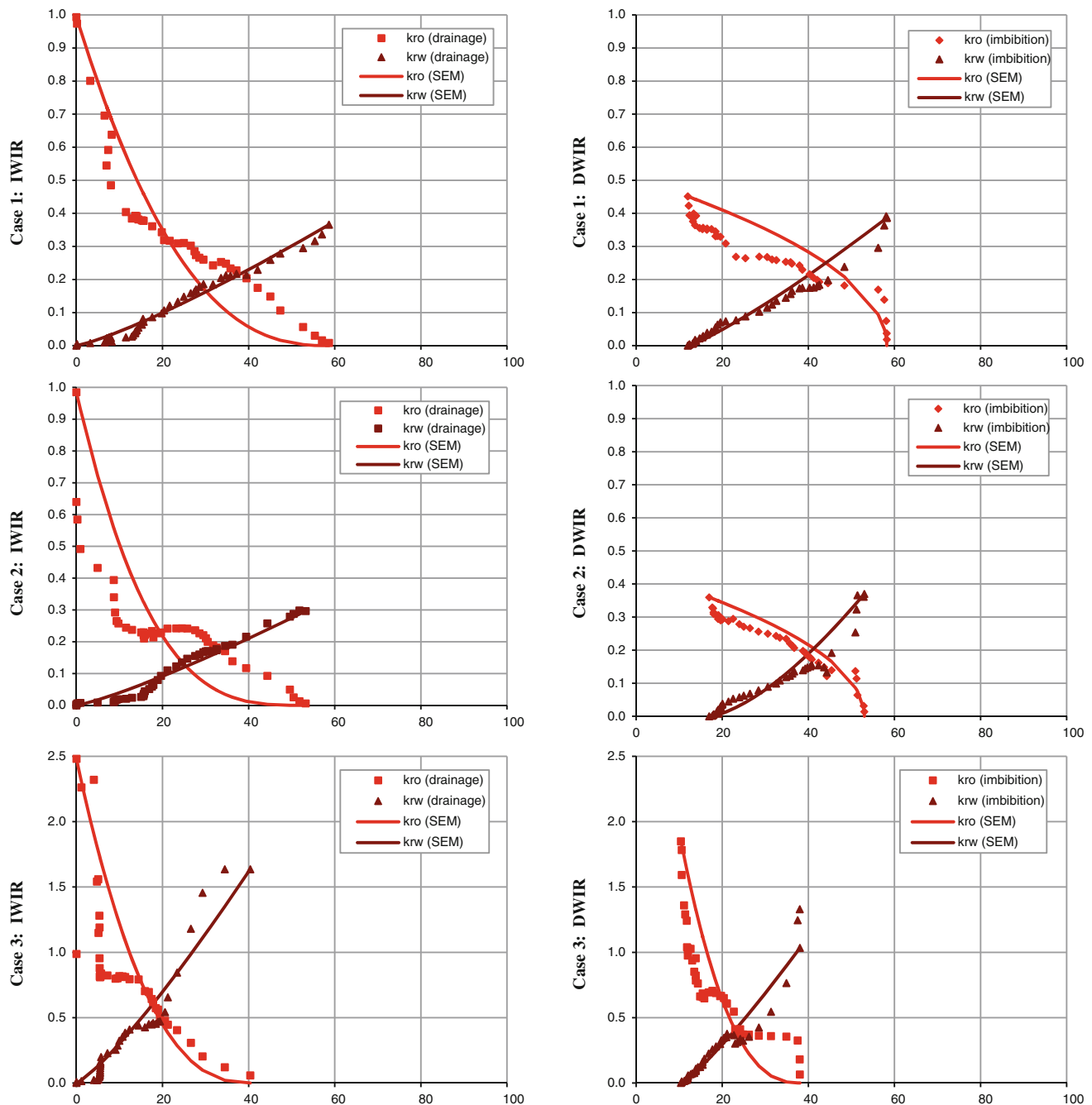


Fig. 21 SEM fits for IWIR and DWIR relative permeability curves with respect to oil and water for Cases 1 (horizontal), 2 (90° up-dip), and 3 (90° down-dip). Relative permeability is on the y-axis (fraction) and water saturation is on the x-axis (%)

to fit the IWIR and DWIR experimental data. The SEM is given by:

$$k_{ro} = k_{ro}^* (1 - S_e)^{e_o} \quad (8)$$

$$k_{rw} = k_{rw}^* (S_e)^{e_w} \quad (9)$$

$$S_e = \frac{(S_w - S_{wi})}{(1 - S_{wi} - S_{or})} \quad (10)$$

where e_o and e_w are fitting parameters for the oil and water relative permeabilities, respectively. k_{ro}^* and k_{rw}^* are defined differently for IWIR and DWIR processes. For the IWIR period, k_{ro}^* is the relative permeability to oil at the initial water saturation, S_{wi} ,

$$k_{ro}^* = k_{ro}(S_{wi});$$

whereas k_{rw}^* is the relative permeability to water at the residual oil saturation, S_{or} ,

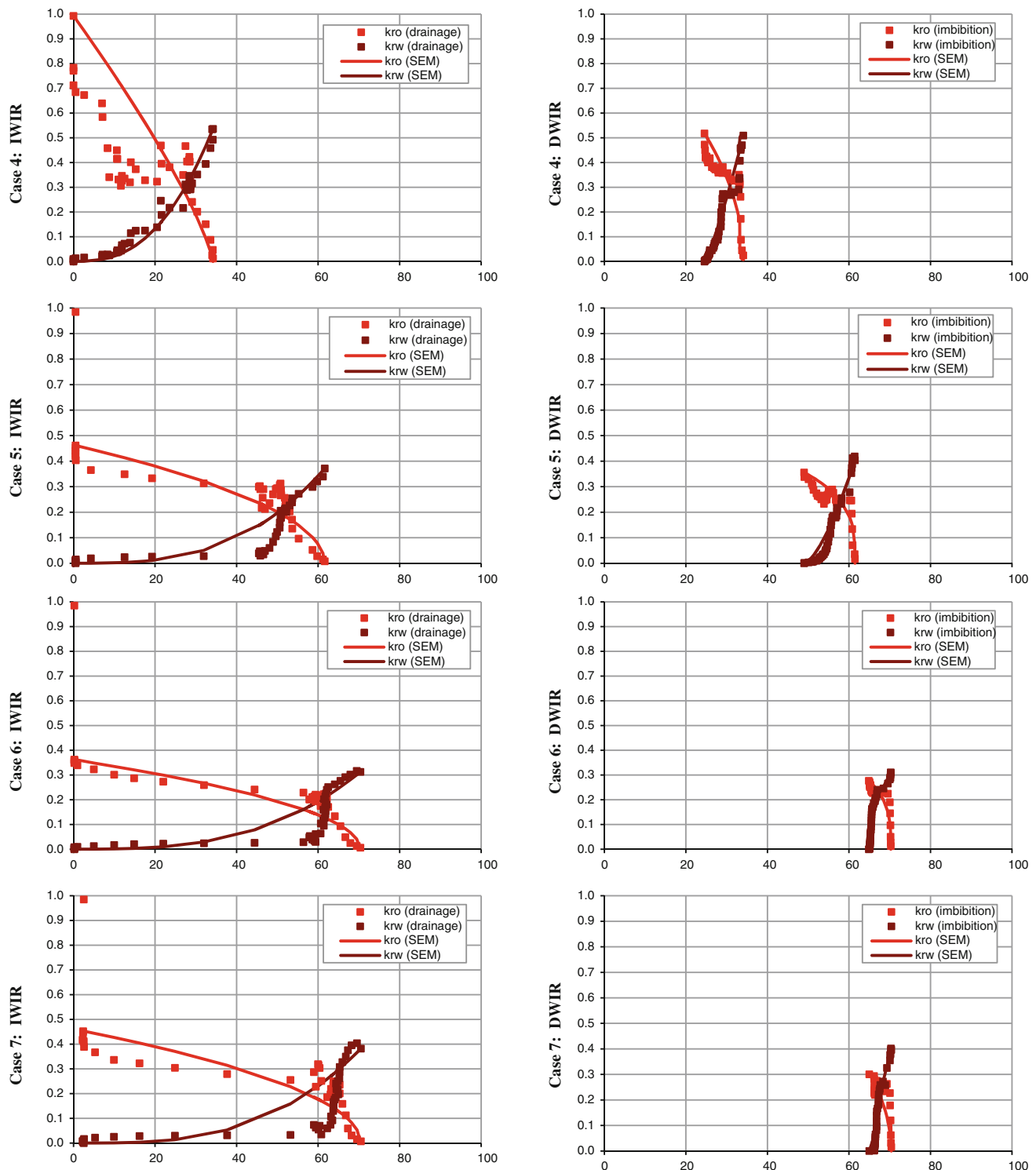


Fig. 22 Cases 4 (horizontal), 5 (30°), 6 (60°), and 7 (90°). History matching IWIR (drainage) and DWIR (imbibition) relative permeability to oil and water with up-dip flow direction and varying fracture

$$k_{rw}^* = k_{rw}(S_{or})$$

however, for the DWIR period, k_{ro}^* is the relative permeability to oil at the irreducible water saturation, S_{wr} ,

orientation with the saturation exponent model (SEM). Relative permeability is on the y-axis (fraction) and water saturation is on the x-axis (%)

$$k_{ro}^* = k_{ro}(S_{wr})$$

and k_{rw}^* is the relative permeability to water at the initial water saturation, S_{wi} .

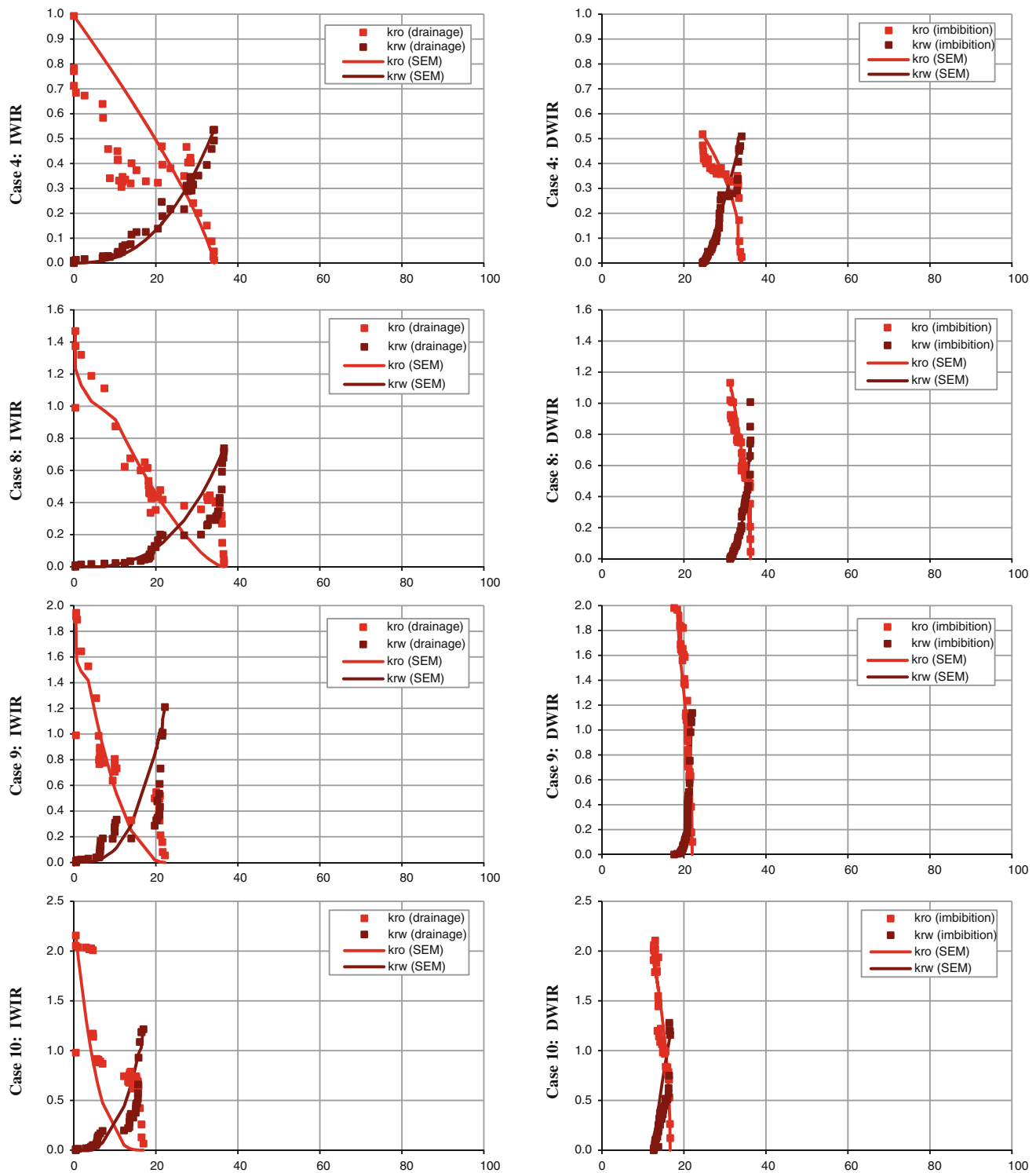


Fig. 23 Cases 4 (horizontal), 8 (30°), 9 (60°), and 10 (90°). History matching IWIR (drainage) and DWIR (imbibition) relative permeability to oil and water with down-dip flow direction and varying

fracture orientation with the saturation exponent model (SEM). Relative permeability is on the y-axis (fraction) and water saturation is on the x-axis (%)

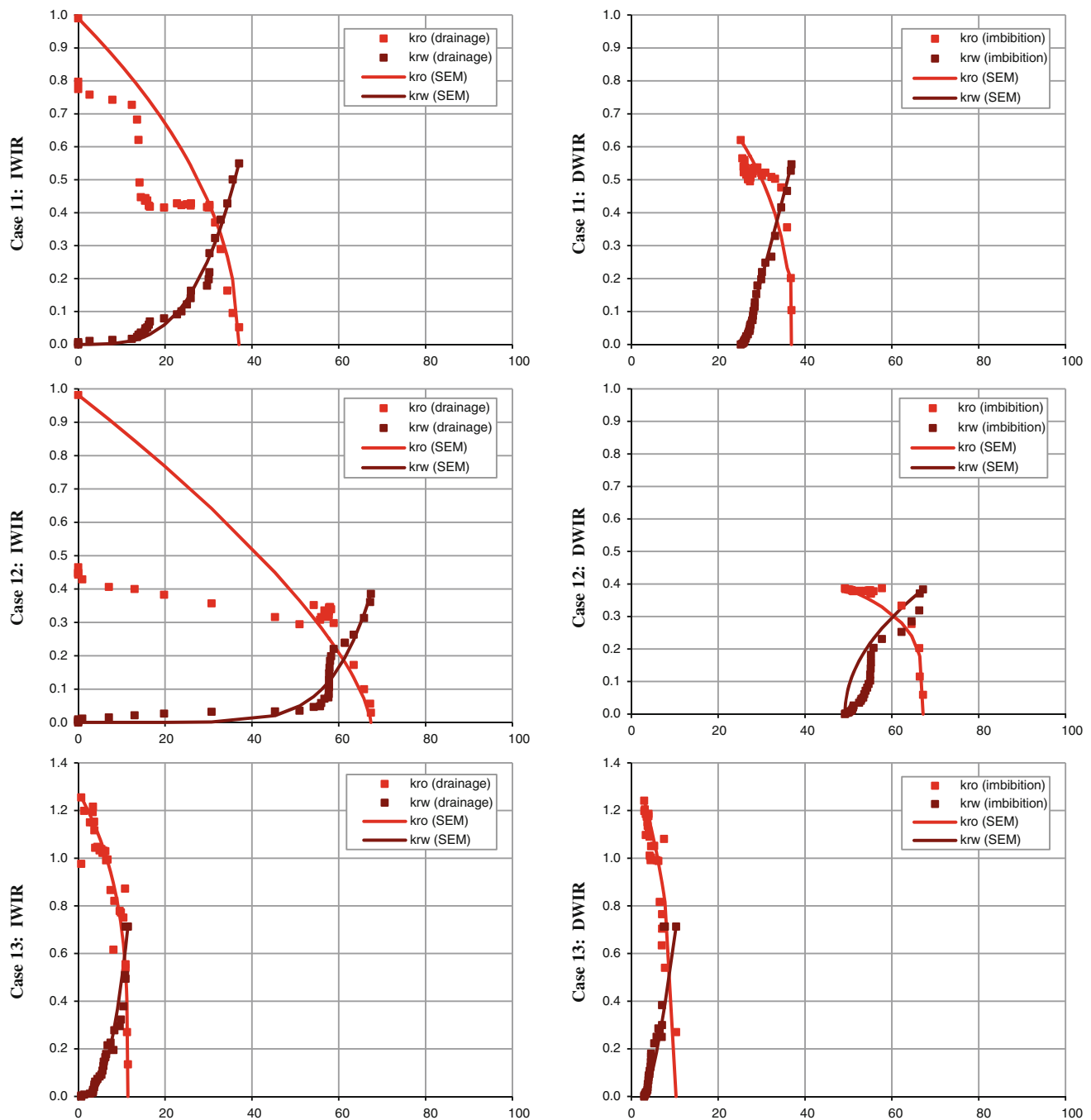


Fig. 24 Cases 11 (horizontal), 12 (90° up-dip), and 13 (90° down-dip). History matching IWIR (drainage) and DWIR (imbibition) relative permeability to oil and water with varying fracture orientation

$$k_{rw}^* = k_{rw}(S_{wi}).$$

Figures 21, 22, 23 and 24 show the best-fit curves generated by the SEM versus the experimental relative permeability data for Cases 1–3, Cases 4–10, and Cases 11–13.

Fourar et al. (1993), and Pan et al. (1996) used the homogenous single-phase approach to fit their

and flow direction with the saturation exponent model (SEM). Relative permeability is on the y-axis (fraction) and water saturation is on the x-axis (%)

experimental data. For the case of laminar flow conditions ($Re_m < 1,000$), the pressure gradient is:

$$\Delta p = -2C\mu_m V_m \frac{L}{D_h^2} \quad (11)$$

where C is an impedance parameter, which is a friction factor that is determined experimentally, and L is the length

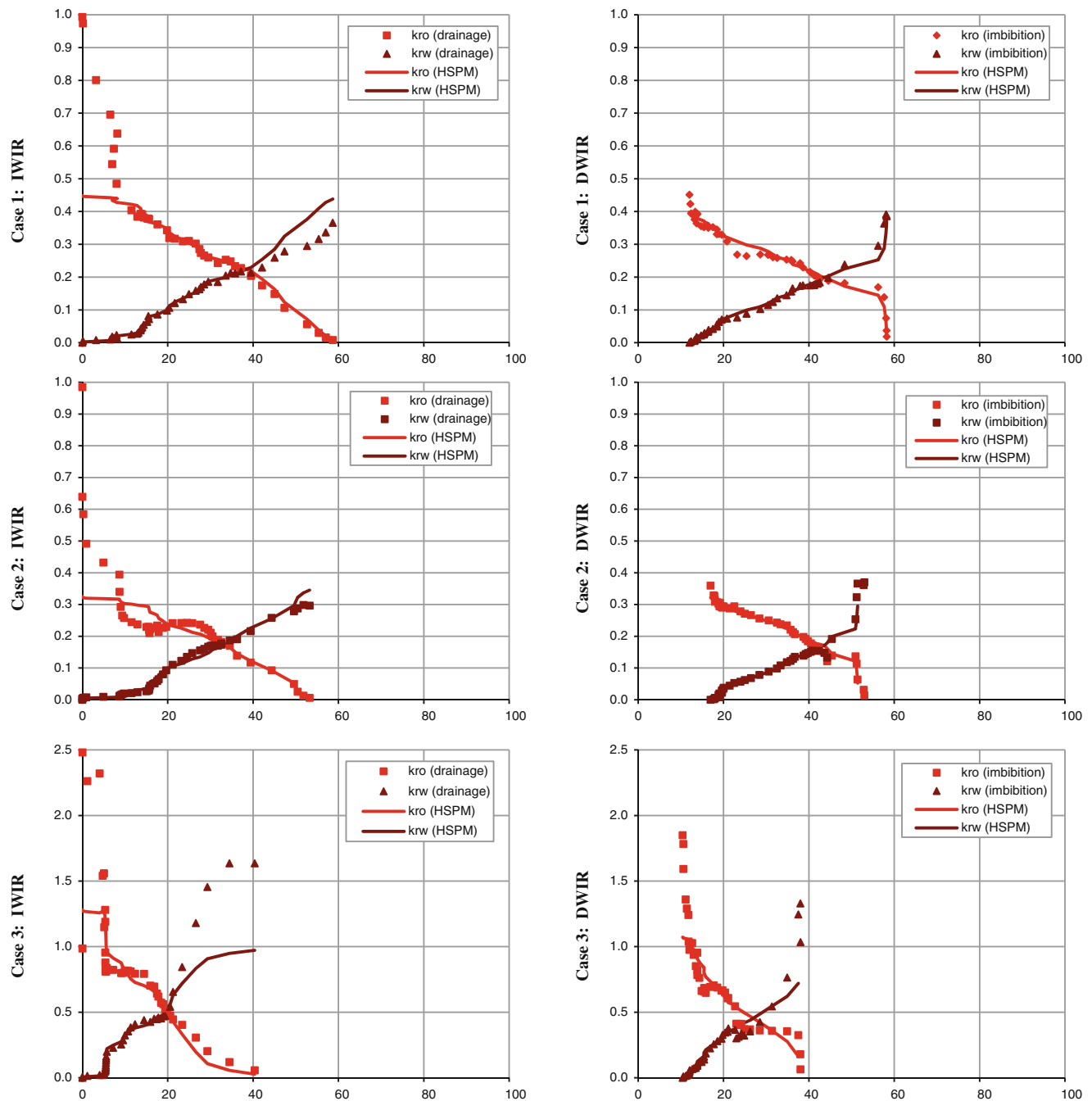


Fig. 25 Cases 1 (horizontal), 2 (90° up-dip), and 3 (90° down-dip). History matching IWIR (drainage) and DWIR (imbibition) relative permeability to oil and water with varying fracture orientation and

flow direction data fitting with homogeneous single-phase model (HSPM). Relative permeability is on the y-axis (fraction) and water saturation is on the x-axis (%)

of the test section. The mean superficial velocity of the two-phase mixture is as follows:

$$V_m = \frac{Q_o + Q_w}{A} \quad (12)$$

where the viscosity of the mixture, μ_m , is defined:

$$\mu_m = \frac{\mu_o Q_o + \mu_w Q_w}{Q_o + Q_w} \quad (13)$$

and the hydraulic diameter of the fracture, D_h , is calculated as follows:

$$D_h = \frac{4A}{\pi} = 2a \quad (14)$$

where, A is the cross-sectional area open to flow and a is the fracture gap (aperture). As stated earlier, Eq. (11) is valid for laminar flow conditions (when $n = 1$). The

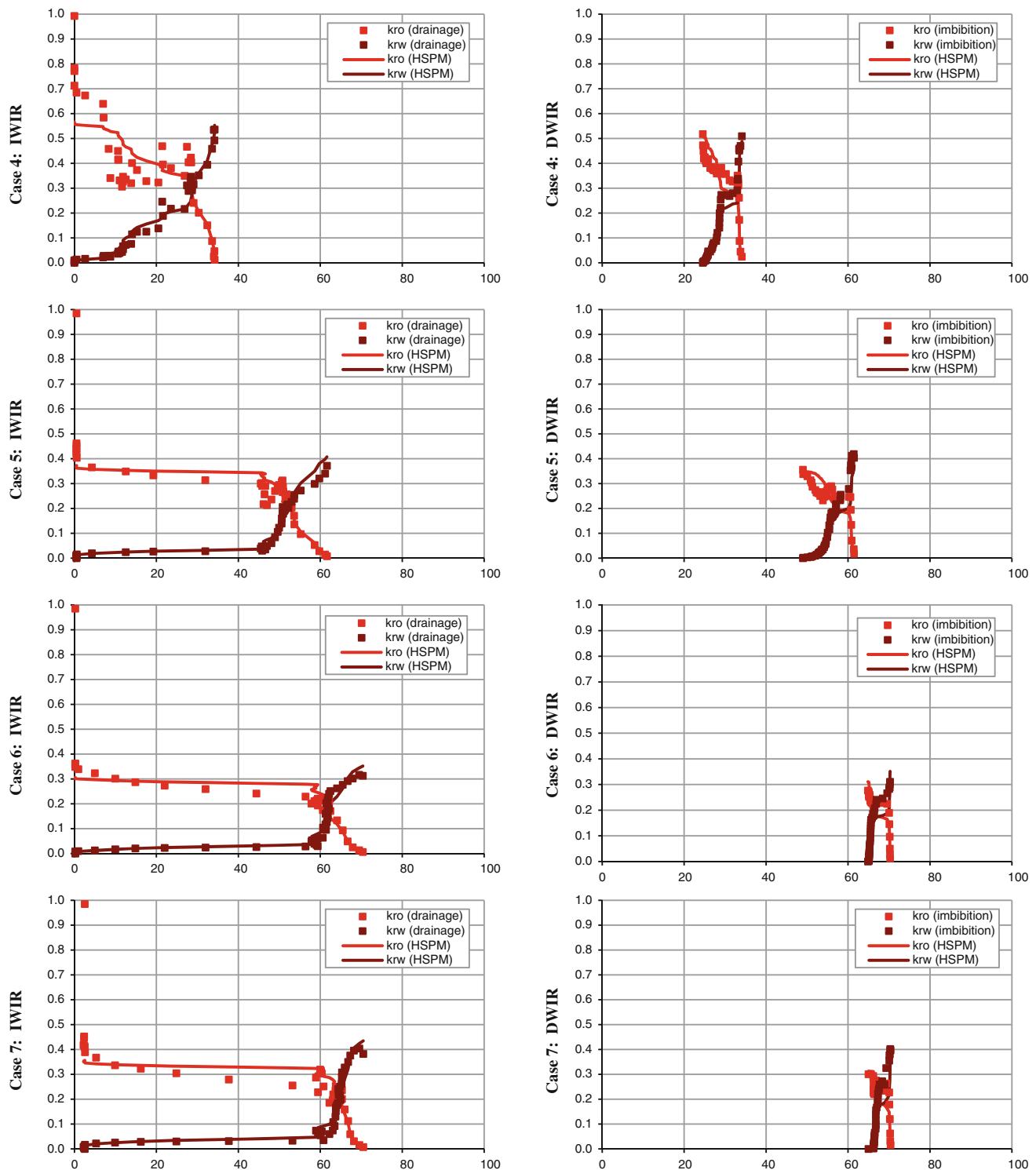


Fig. 26 Cases 4 (horizontal), 5 (30°), 6 (60°), and 7 (90°). History matching IWIR (drainage) and DWIR (imbibition) relative permeability to oil and water with up-dip flow direction and varying fracture

orientation with the homogeneous single-phase model (HSPM). Relative permeability is on the y-axis (fraction) and water saturation is on the x-axis (%)

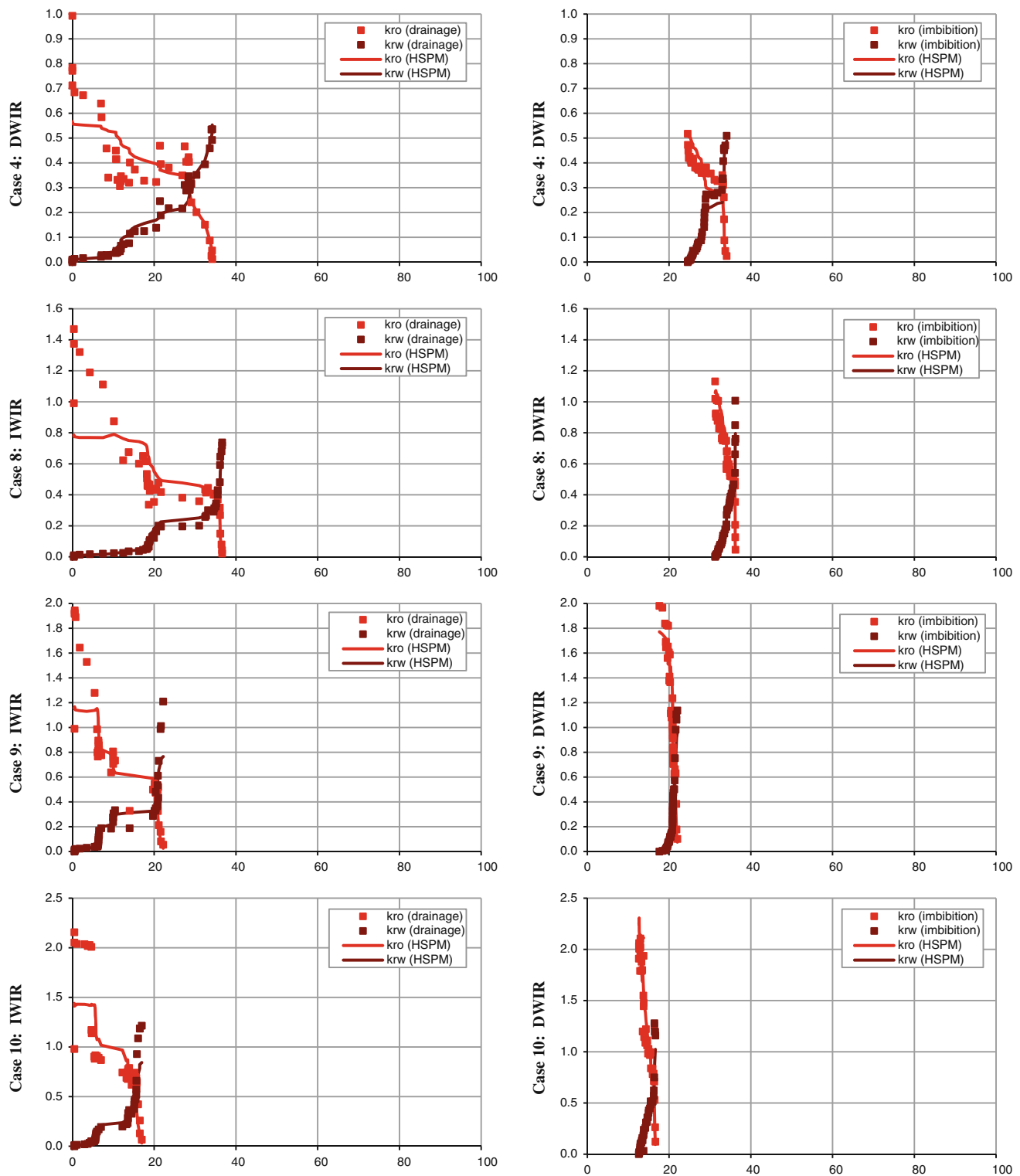


Fig. 27 Cases 4 (horizontal), 5 (30°), 6 (60°), and 7 (90°). History matching IWIR (drainage) and DWIR (imbibition) relative permeability to oil and water with down-dip flow direction and varying

fracture orientation with the homogeneous single-phase model (HSPM). Relative permeability is on the y-axis (fraction) and water saturation is on the x-axis (%)

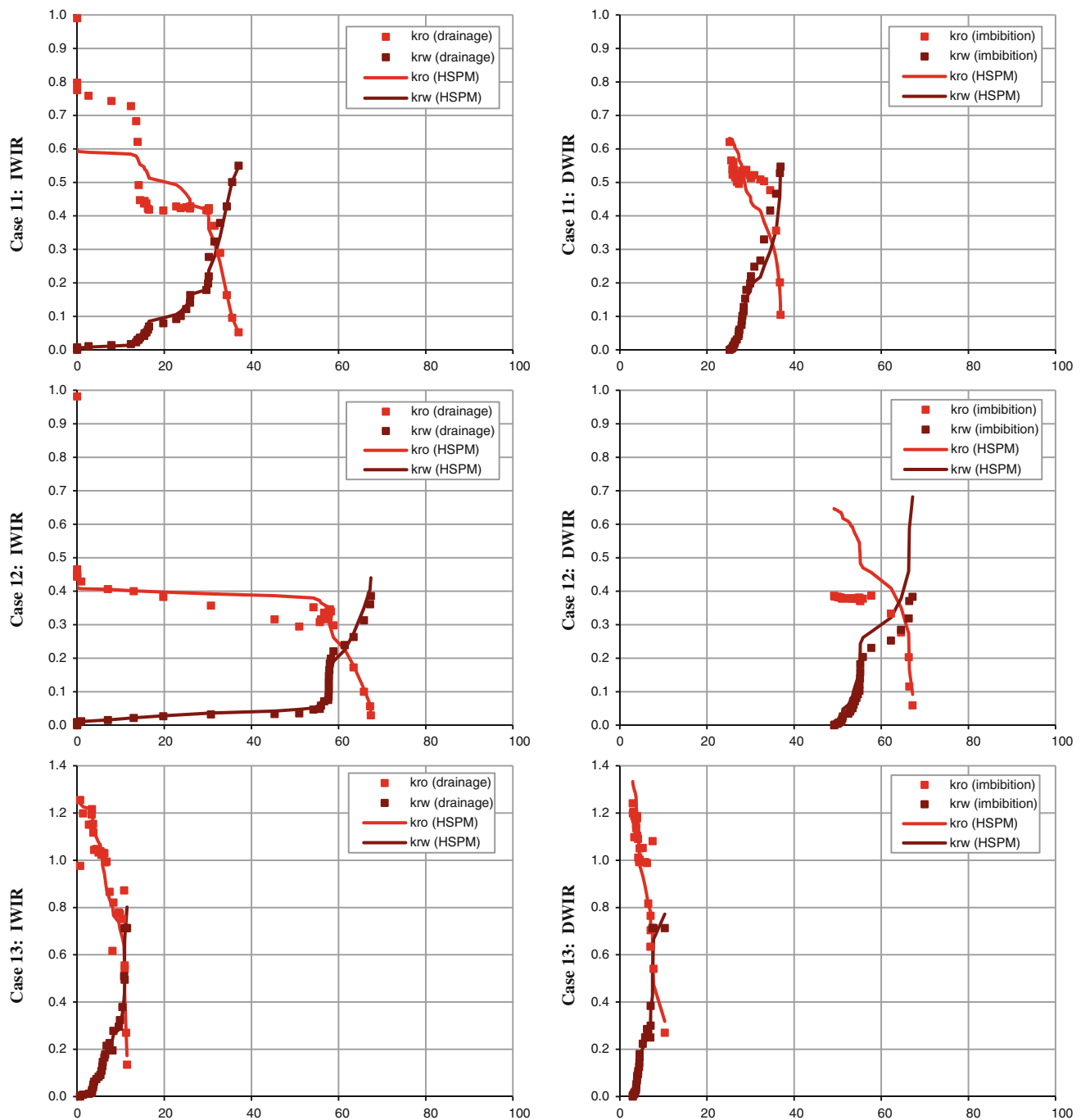


Fig. 28 Cases 11 (horizontal), 12 (90° up-dip), and 13 (90° down-dip). History matching IWIR (drainage) and DWIR (imbibition) relative permeability to oil and water with varying fracture orientation

and flow direction with the homogeneous single-phase model (HSPM). Relative permeability is on the y-axis (fraction) and water saturation is on the x-axis (%)

friction and mixture Reynolds' number can be calculated as follows:

$$\psi = \frac{C}{Re_m^n} \quad (15)$$

$$Re_m = \frac{D_h \rho_m V_m}{\mu_m} \quad (16)$$

The relative permeabilities to oil and water can be found from Eqs. (5) and (6), respectively, from predicted pressure

values obtained from the HSPM. Figures 25, 26, 27 and 28 show fits of the experimental data determined by the HSPM for Cases 1–3, Cases 4–10, and Cases 11–13.

Discussion

Cases 1–3

The IWIR relative permeability data shown in Fig. 4 shows that only the 90° inclination angle with down-dip flow direction exhibited greater than unity relative permeability. There is also a clear shift to lower water saturation of the crossover point. Similar observations can be made when examining the DWIR data displayed in Fig. 5. At the end of the IWIR process, the maximum water saturation reached is equal to approximately 60 %; this was found to be less with the up- and down-dip 90° inclination cases (Cases 2 and 3). However, by the end of the DWIR process, all three orientations exhibited an irreducible water saturation of about 10 %.

Cases 4–10

The IWIR up-dip relative permeability curves (Cases 4–7) are shown in Fig. 5. Compared to the data measured from the horizontal orientation (Case 4), the relative permeability curves, gradually, shift to higher water saturation as the inclination angle is raised. For Cases 8–10, the down-dip IWIR relative permeability curves also shift to lower water saturation with increasing inclination angle, but the shift is less dramatic, as depicted in Fig. 6. Also, the relative permeability to oil shows greater than unity values; this is pronounced for the results at 60 and 90° inclination angles. The DWIR relative permeability data for Cases 4–7 and 8–10 are depicted in Figs. 7 and 8, respectively. The up-dip DWIR curves for Cases 4–7 shown in Fig. 7 exhibit similar behavior to the IWIR ones but they are shifted to higher water saturation, higher end-point water saturations, and higher irreducible water saturations with increasing inclination angles. Examining the down-dip DWIR curves for Cases 8–10 displayed in Fig. 8, the opposite behavior of the up-dip DWIR curves is noticed. The curves are shifted to lower water saturation, lower end-point water saturation, and lower irreducible water saturations with increasing inclination angles.

Cases 11–13

Figures 9 and 10 depict the up- and down-dip IWIR and DWIR relative permeability curves with respect to oil and water, respectively. Figure 9 shows that for up-dip flow direction (Case 12), the IWIR relative permeability curves

cover a wider water saturation range with higher end-point water saturation, but with lower relative permeability values compared to the horizontal case (Case 11). However, in the case of down-dip flow direction, Case 13, the curves cover a smaller water saturation range with lower end-point water saturation, and greater than unity relative permeability to oil.

The DWIR data is shown in Fig. 10. The relative permeability data is clustered in a small range of water saturations. Similar to the IWIR data, the relative permeability curves shift to lower water saturations for down-dip flow and to higher water saturation for up-dip flow. The relative permeability to oil is lower than its counterparts in the IWIR process.

Saturation exponent model (SEM)

Table 3 lists the SEM and HSPM matching parameters used to fit the experimental relative permeability data for all cases. Figure 20 shows the SEM fit versus the experimental data for Cases 1 through 3. Clearly, the SEM was not able to fit the increasing water injection rate relative permeability to oil (Fig. 20, IWIR). However, the DWIR relative permeability to oil (Fig. 20, DWIR) was better fitted. The water relative permeability curves were better fitted than the oil ones.

Figure 21 shows up-dip IWIR and DWIR relative permeability data against the SEM fit: A.1 to D.1 show the IWIR data (Cases 4–7) whereas A.2 to D.2 show the DWIR data (Cases 4–7). The results show that the SEM was not able to provide a good fit. The increasing water injection rate curves show a sharp increase or decrease that could not be represented by the SEM. The SEM fit to the IWIR and DWIR down-dip cases' (Cases 8–10) relative permeability data is shown in Fig. 22. The SEM was able to fit the increasing water injection rate data except for the 90° inclination angle (D.1). The SEM exhibited better fitting to the DWIR relative permeability data with respect to oil and water. Figure 23 plots the results for Cases 11–13. For these cases, the SEM fits the experimental data reasonably well.

Homogenous single-phase model (HSPM)

Figure 24 displays the HSPM fits for Cases 1–3. The model did not provide good fits to the low-water saturation oil relative permeability data (A.1 to C.1). Also, the model poorly fitted the first data points of the relative permeability to oil and last points of the relative permeability to water in both IWIR (C.1) and DWIR (C.2) of the 90° inclination with down-dip flow (Case 3). As Table 3 shows, the 90° orientation with up-dip flow showed slight increase in the impedance parameter, C , values compared to the ones from

horizontal orientation. On the other hand, the 90° orientation with down-dip flow showed lower impedance parameter values compared to the horizontal ones. Pan et al. (1996) indicated that the magnitude of the impedance parameter is related to how well-mixed is the two-phase flow. The higher the degree of mixing of the two phases, the higher the impedance parameter value. Pan (1999) has not reported impedance parameter values for the rough-walled gap experiments. However, phase segregation was not experimentally observed either in the roughened- or smoothened-wall gaps despite of the relatively low-impedance parameter values obtained from various experiments (Pan et al. 1996; Pan 1999; Alturki et al. 2013). These relatively low-impedance values could be attributed to formation of water channels that been established and persisted throughout the experiment. Table 3 summarizes the experimental values obtained from the rough-walled gaps.

As shown in Fig. 25, HSPM fits to Cases 4–7 for IWIR and DWIR relative permeability curves with up-dip flow are good. In some cases, for example Case 7 (D.1), the model slightly overpredicted the relative permeability to oil. For both IWIR and DWIR periods, the impedance parameter values increased by the same relative increase in the inclination angle in the up-dip flow cases (Cases 4–7). The fits to the down-dip IWIR and DWIR periods of Cases 8–10 are plotted in Fig. 26. Similarly, the model did not fit the first set of the relative permeability to oil in the IWIR period (A.1 to D.1), and the last points in the DWIR period (A.2 to D.2). The model overpredicts the differential pressure values which resulted in lower relative permeability to oil. The impedance parameter values decreases with increasing inclination angle in down-dip flow direction cases (Cases 8–10).

Figure 27 illustrates the HSPM fit to relative permeability data for Cases 11–13. The results are similar to that of Cases 1–10.

Conclusions

Randomly roughened gaps in Hele-Shaw cells were used to investigate the effects of wall roughness, gap orientation, and fluids flow direction within rough-walled oil-wet gaps on oil–water phase interference as reflected by two-phase relative permeability to oil and water. The apparatus serves as a simple model of a rough-walled fracture as would be found in oil reservoirs. The experimental relative permeabilities from the experiments show the effect of the aforementioned factors and demonstrate that phase interference occurs. As it has been observed from previous work with smooth-walled gaps, the relative permeability to oil and water for down-dip

flow direction increases with increasing gap inclination. However, raising the gap inclination with up-dip flow direction decreases the relative permeability. The relative permeability to oil and water for cases with 0.0381 cm gap is in general lower than that found in the cases with 0.125 cm gap. The tortuosity and complexity as measured by the fractal dimension of the water channels could explain such behavior: the smaller gap promotes more complex phase interference which lowers the mobility of both phases. Greater than unity relative permeability data was observed with down-dip flow direction illustrating the benefit of gravity on the flows. This implies that potentially the oil phase was “lubricated” by the water phase. Multiple flow states at the same oil-to-water injection ratio were observed for all cases studied. The experimental data was fitted to the saturation exponent and homogenous single-phase models. The results of the fits revealed that the SEM could be used to smoothen the scattered experimental data providing relative permeability curves that can be used for fracture flow reservoir engineering calculations. The homogeneous single-phase model fitted the experimental data to a reasonable extent but in some cases it provided poor estimates of the pressure gradient.

Acknowledgments The authors acknowledge financial support from Saudi ARAMCO, and the Department of Chemical and Petroleum engineering for facilitating the laboratory work.

Open Access This article is distributed under the terms of the Creative Commons Attribution License which permits any use, distribution, and reproduction in any medium, provided the original author(s) and the source are credited.

References

- Aguilera R (1995) Naturally fractured reservoirs, 2nd edn. Pennwell, Tulsa
- Alturki AA, Maini BB, Gates ID (2013) The effect of fracture aperture and flow rate ratios on two-phase flow in smooth-walled single fracture. *J Pet Explor Prod Technol* 3(2):119–132
- Chen C-Y (2005) Liquid–gas relative permeabilities in fractures: effects of flow structures, phase transformation and surface roughness, Ph.D. thesis, Stanford University, Stanford, California, USA
- Chen C-Y, Horne RN (2004) Experimental study of liquid flow structures effects on relative permeabilities in a fracture. *Water Resour Res* 40:W08301. doi:10.1029/2004WR003026
- Chen C-Y, Horne RN (2006) Two-phase flow in rough walled fractures: experiments and a flow structure model. *Water Resour Res* 42:W03430. doi:10.1029/2004WR003837
- Diomampo GP (2001) Relative permeability through fractures, M.Sc. thesis, Stanford University, Stanford
- Fourar M, Bories S (1995) Experimental study of air–water two-phase flow through a fracture (narrow channel). *Int J Multiph Flow* 21(4):621–637

- Fourar M et al (1993) Two-phase flow in smooth and rough fractures: measurement and correlation by porous-medium and pipe flow models. *Water Resour Res* 29(11):3699–3708
- Pan X (1999) Immiscible two-phase flow in a fracture, Ph.D. thesis, Department of Chical and Petroleum Engineering, University of Calgary, Calgary, Alberta, Canada
- Pan X, Wong RC, Maini BB (1996) Steady-state two-phase in a smooth parallel fracture, paper 96-39. The Petroleum Society in Calgary, Alberta
- Persoff P, Pruess K (1995) Two-phase flow visualization and relative permeability measurement in naturally rough-walled rock fractures. *Water Resour Res* 31(5):117–1186
- Shad S, Maini B, Gates I (2010) Effect of fracture and flow orientation on two-phase flow in an oil-wet fracture: relative permeability curves and flow structure. SPE 132229. ISBN 9781617388866